Regulation of RNG105/caprin1 dynamics by pathogenic cytoplasmic FUS and TDP-43 in neuronal RNA granules modulates synaptic loss

Tomoyo Horio [a,b], Yui Ishikura [a,b], Rie Ohashi [a,b,c,d], Nobuyuki Shiina [a,b,c,*,1]

[a] Laboratory of Neuronal Cell Biology, National Institute for Basic Biology, Okazaki, Aichi 444-8585, Japan
[b] Department of Basic Biology, Graduate University for Advanced Studies (SOKENDAI), Okazaki, Aichi 444-8585, Japan
[c] Exploratory Research Center on Life and Living Systems (ExCELLS), National Institutes of Natural Sciences, Okazaki, Aichi 444-8585, Japan
[d] Life Science Research Center, University of Toyama, Toyama, Toyama 930-0194, Japan

ABSTRACT

In neurodegenerative diseases, the condensation of FUS and TDP-43 with RNA granules in neurons is linked to pathology, including synaptic disorders. However, the effects of FUS and TDP-43 on RNA granule factors remain unclear. Here, using primary cultured neurons from the mouse cerebral cortex, we show that excess cytoplasmic FUS and TDP-43 accumulated in dendritic RNA granules, where they increased the dynamics of a scaffold protein RNG105/caprin1 and dissociated it from the granules. This coincided with reduced levels of mRNA and translation around the granules and synaptic loss in dendrites. These defects were suppressed by non-dissociable RNG105, suggesting that RNG105 dissociation mediated the defects. In contrast to the model where FUS and TDP-43 co-aggregate with RNA granule factors to repress their activity, our findings provide a novel pathogenic mechanism whereby FUS and TDP-43 dissociate RNA scaffold proteins from RNA granules which are required for local translation that regulates synapse formation.

1. Introduction

Amyotrophic lateral sclerosis (ALS) and frontotemporal dementia (FTD) are progressive and incurable neurodegenerative diseases with a clinical and pathological continuum involving motor, behavior, and cognitive dysfunction [1–3]. A contributing feature of these diseases is decreased synaptic density and loss of mature dendritic spines before the neuronal loss [4–10]. A common histopathological hallmark of ALS and FTD neurons is the cytoplasmic aggregation of fused-in-sarcoma (FUS) and TAR DNA binding protein 43 (TDP-43) [3,11], RNA-binding proteins (RBPs) normally located in the nucleus and play multiple functions in RNA metabolism [12,13]. This change in localization is enhanced by disease-associated mutations in FUS and TDP-43 and is believed to alter the functions of FUS and TDP-43 in the nucleus and enable the toxic properties of cytoplasmic aggregation [3,14,15]. Not only those mutations but also increased expression of FUS and TDP-43, even in the absence of mutations, causes cytoplasmic aggregation and disease phenotypes in transgenic mice and is associated with disease in human patients [11,16–20].

FUS and TDP-43 are prone to undergo liquid-liquid phase separation (LLPS) by multivalent intermolecular interactions through their RNA-binding domains (RBDs) and prion-like domains (PrLDs), the latter of which are intrinsically disordered regions (IDRs) with low sequence complexity [21,22]. Through LLPS, they co-assemble in the cytoplasm with neuronal RNA granule components, such as IDR-containing RBPs, mRNAs, and ribosomes, many of which are common to stress granules [23–27].
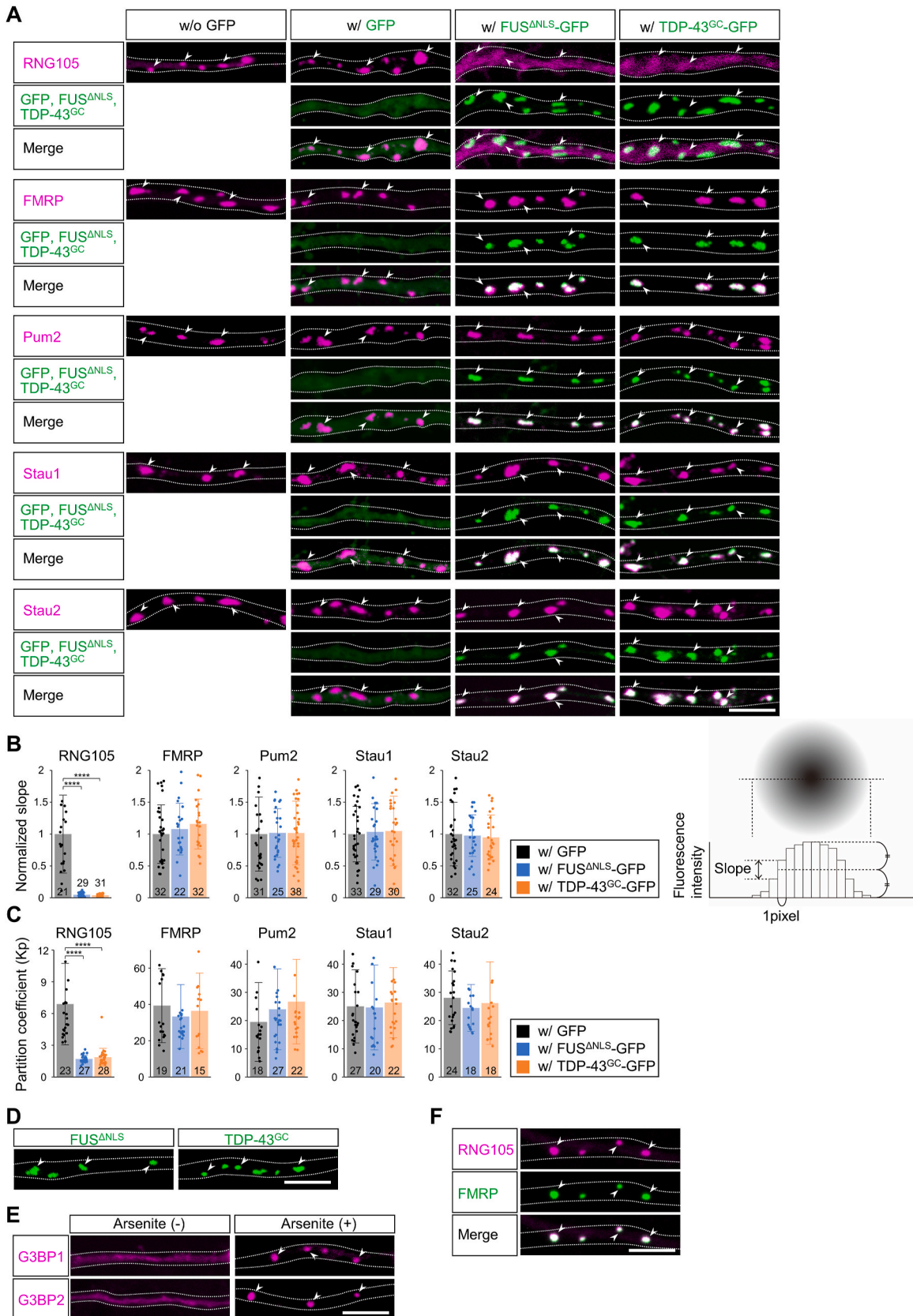
Fig. 1. Accumulation of FUS$^{\Delta NLS}$ and TDP-43^{G348C} in RNA granules dissociates RNG105 from the granules. (A) Localization of mRFP1-tagged RBPs to RNA granules in dendrites of cultured neurons, and the effect of expression of GFP-tagged FUS$^{\Delta NLS}$ and TDP-43^{G348C} (TDP-43^{GC} for simplicity) on the RNA granule localization of the RBPs. Arrowheads indicate representative RNA granules in the dendrites. The dotted lines outline the dendrites. **(B)** The degree of accumulation of RBPs in dendritic RNA granules was assessed by the slope of RBP fluorescence in the granules. The method for measuring the slope is shown in the schematic on the right. The slope was normalized by the slope of the RBP without expression of FUS$^{\Delta NLS}$ or TDP-43^{GC}. **(C)** The granule/cytoplasm partition coefficient of RBPs. **(D)** Localization of GFP-tagged FUS$^{\Delta NLS}$ and TDP-43^{GC} to granules in dendrites of neurons expressing each of them alone. **(E)** Localization of mRFP1-tagged G3BP1 and G3BP2 to granules in dendrites with 60-min exposure to 1 mM arsenite. **(F)** Co-localization of RNG105-mRFP1 and FMRP-GFP in dendritic RNA granules in neurons co-expressing them. Scale bars, 5 μm. The data are represented by scatter plots of the individual values, stated as the mean ± S.D. The number of granules analyzed from three independent cultures from different mice is shown in the graph. ****p < 0.001, Tukey-Kramer test after one-way ANOVA. See also Figs. S1 and S2.

Under normal conditions, only a small fraction of FUS and TDP-43 is localized to RNA granules and may function for dendritic transport of mRNAs and synaptic stimulation-dependent local translation [3,12,28,29]. Spatiotemporal regulation of translation in RNA granules is key to stimulation-dependent synaptic plasticity and long-term memory formation [30–32]. However, aberrant cytoplasmic translocation of FUS and TDP-43 and their accumulation in RNA granules are thought to cause the RNA granules to harden and lose their function [22,25,29,33]. This model derives from the fact that phase-separated FUS and TDP-43 are prone to transition into hydrogels and solids [34–37]. Nevertheless, it is unclear whether the FUS and TDP-43 accumulation affects the dynamics of other RNA granule components that normally regulate RNA granule function, and whether such dynamics changes are related to the FUS- and TDP-43-induced defects.

In this study, we investigated the effects of FUS and TDP-43 overexpression and accumulation in RNA granules on the dynamics of IDR-containing scaffold RBPs, including FMRP, Staufen1 (Stau1), Stau2, Pumilio2 (Pum2), and RNG105 (a.k.a. caprin1) [38,39], in primary cultured neurons from the mouse brain. The most notable effects were increased dynamics of RNG105 in RNA granules and its dissociation from the granules. RNG105 dissociation was associated with decreased mRNA levels and translation activity in/near the granules and synaptic loss in dendrites. These defects were restored by non-dissociable RNG105, where its RBD was replaced with the RBDs of other scaffold RBPs. These findings provide insight into a novel regulatory mechanism by which FUS and TDP-43 induce neuronal dysfunction by dissociating scaffold proteins from RNA granules.

2. Results

2.1. FUS and TDP-43 accumulation in RNA granules increases the dynamics of RNG105 and its dissociation from the granules

FUS and TDP-43 mutants associated with ALS and FTD are often characterized by accumulation and aggregation in the cytoplasm. Human FUS$^{\Delta NLS}$ and TDP-43^{G348C} are examples of such mutants ([40–42]), and their expression in transgenic mice has been reported to develop age-related pathological, biochemical, and behavioral changes, including learning and memory impairment reminiscent of human ALS and FTD [43,44]. These mutants were expressed as GFP-tagged proteins in primary cultured neurons from the mouse cerebral cortex. Immunostaining analysis revealed their higher expression than endogenous FUS and TDP-43, especially in the cytoplasm (Fig. S1). We then investigated the effects of their expression on the dynamics of mRFP1-tagged RNA granule scaffold RBPs in dendrites.

Expression of individual RBPs, including RNG105, FMRP, Pum2, Stau1, Stau2, FUS$^{\Delta NLS}$, and TDP-43^{G348C}, induced the formation of granules in the cell body and dendrites (Fig. 1A and D). These granules had a smooth surface, resembling liquid-like properties, although some had a rough surface, characteristic of granules formed by RBPs with solid-like properties [45]. The exceptions were G3BP1 and G3BP2, which formed granules only when neurons were stressed with arsenite (Fig. 1E). These results suggested that the granules formed by G3BP1/2 were stress granules, whereas those formed by the other RBPs in the unstressed state were neuronal RNA granules. Accordingly, subsequent experiments were conducted without stress, excluding G3BP1/2.

Co-expression of FUS$^{\Delta NLS}$ and TDP-43^{G348C} with FMRP, Pum2, and Stau1/2 resulted in their co-assembly into granules (Fig. 1A). The degree of their accumulation in the granules, as determined by the slope of the fluorescence peak of individual granules, was not affected by FUS$^{\Delta NLS}$ or TDP-43^{G348C} co-assembly (Fig. 1B). In contrast, the accumulation of RNG105 in granules was significantly reduced, with a more diffuse distribution of RNG105 in the dendritic cytoplasm (Fig. 1A and B). Consistently, the granule/cytoplasm partition coefficient of RNG105 was significantly decreased (Fig. 1C), implying an impaired partitioning/retention of RNG105 in the FUS$^{\Delta NLS}$ and TDP-43^{G348C}-rich granules.

Similar experiments conducted with WT FUS and TDP-43 yielded essentially the same results (Figs. S2A–S2C). The similar effects of WT FUS and TDP-43 as the mutants may be due to the fact that overexpressed WT FUS and TDP-43 localized in the cytoplasm in addition to the nucleus and assembled into RNA granules (Fig. S2C). Even if the translocation efficiency of the WT proteins to the cytoplasm is lower than that of the mutants, it may be sufficient to increase RNG105 dynamics if their concentrations in the cytoplasm exceed the saturation for phase separation. These results are reminiscent of the reports suggesting that elevated cytoplasmic concentrations of FUS and TDP-43 are associated with ALS and FTD pathology, even in the absence of disease-associated mutations [3,13].

The dissociation of RNG105 from the granules was not induced by FMRP (Fig. 1F), which reportedly binds to RNG105 and co-phase separates *in vitro* [46,47], confirming that RNG105 can assemble into RNA granules with certain RNA granule RBPs. Collectively, these results indicate that FUS and TDP-43 affect the accumulation of RNG105, but not other RBPs, in RNA granules.

Next, the effects of FUS and TDP-43 on the dynamics of RBPs in the granules were analyzed by fluorescence recovery after
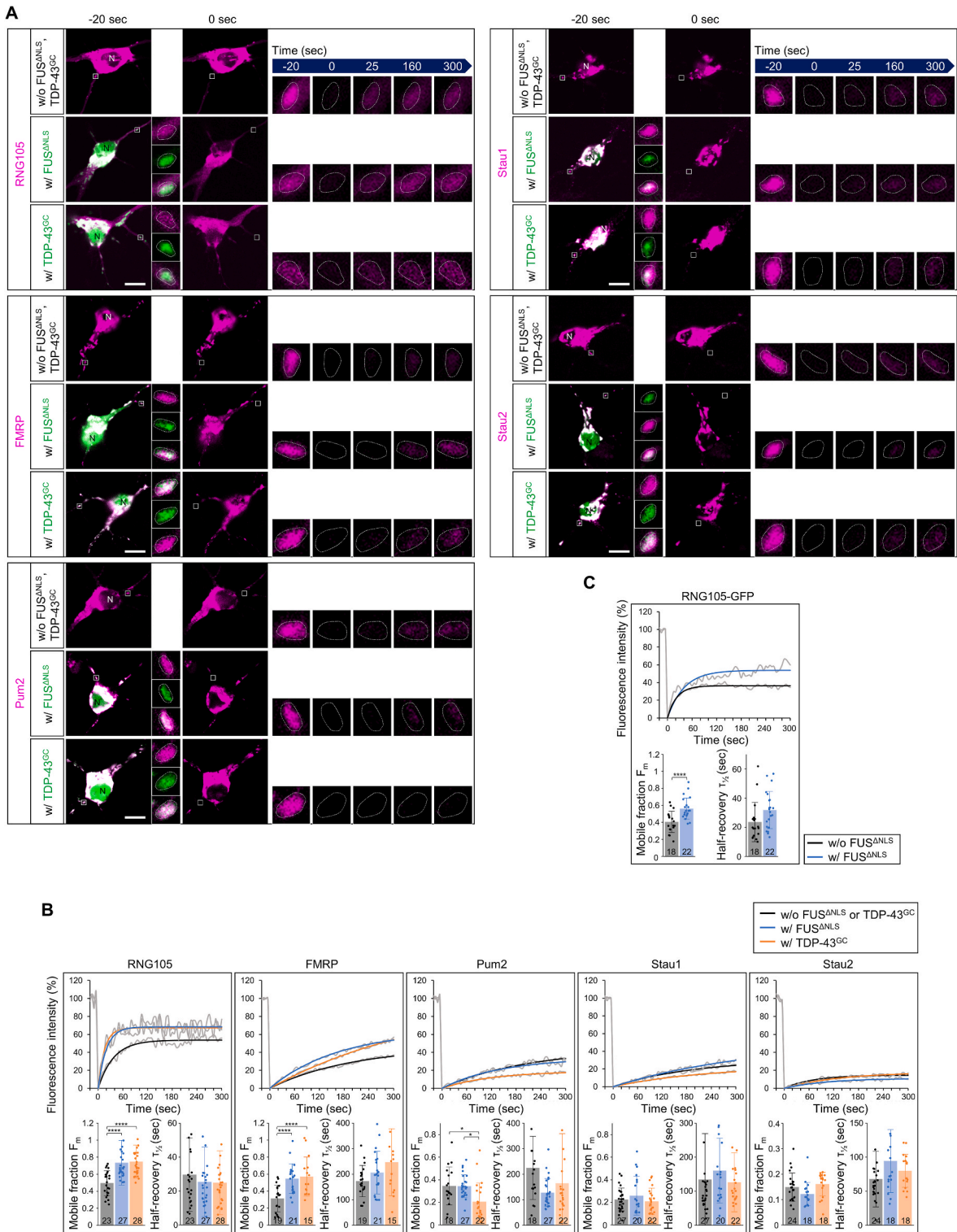
Fig. 2. Accumulation of FUS$^{\Delta NLS}$ and TDP-43^{G348C} causes RNG105 to be more dynamic in RNA granules. (A) Representative time-lapse FRAP images of mRFP1-tagged RBPs in neurons with and without expression of GFP-tagged FUS$^{\Delta NLS}$ or TDP-43^{GC}. The boxed areas containing the dendritic RNA granules analyzed by FRAP are magnified in the insets and the right panels, with the quantified regions surrounded by dotted lines. The boxed dendritic granule area was bleached just before 0 s. Because light exposure was optimized for RNA granules in dendrites, the images of RNA granules in cell bodies and proximal dendrites are overexposed. Representative images of RNA granules in/near cell bodies with lower exposure can be seen in Figs. S1 and S9. *N*, nuclei. Scale bars, 10 μm. (B) Top, representative FRAP curves of RBPs in dendritic RNA granules, and

fitted curves with exponential equations. The gray lines show the measured values. Bottom, the mobile fraction (F_m) and halftime of recovery ($\tau_{1/2}$) extracted from the fitted equations. **(C)** FRAP analysis performed by exchanging the GFP and mRFP1 tags between RNG105 and FUS$^{\Delta NLS}$. The data are represented by scatter plots of the individual values, stated as the mean $\pm$ S.D. The number of granules analyzed from 4 independent cultures is shown in the graph. *p < 0.05, ****p < 0.001, Tukey-Kramer test after one-way ANOVA. See also Fig. S3.

photobleaching (FRAP). The FRAP curve of each experiment was fitted with the exponential equation, from which the mobile fraction (F_m) and half-time of recovery ($t_{1/2}$) were extracted. The results showed that the effects of FUS$^{\Delta NLS}$ and TDP-43^{G348C} on RBPs differed among RBPs. The F_m of Pum2 and Stau1/2 was reduced or not changed, indicating that FUS$^{\Delta NLS}$ and TDP-43^{G348C} reduced or did not affect the mobility of Pum2 and Stau1/2 in RNA granules (Fig. 2A and B). In contrast, FUS$^{\Delta NLS}$ and TDP-43^{G348C} increased the F_m of RNG105 and FMRP (Fig. 2A and B). The increased mobile fraction of RNG105 may be partially due to the reduced partitioning of RNG105 into the granules, as observed at time −20 s (Fig. 2A). Similar experiments performed by exchanging GFP and mRFP1 tags of RNG105 obtained similar results (Fig. 2C), except that RNG105 with the mRFP1 tag tended to be less concentrated in RNA granules than the GFP-tagged version. In addition, experiments with WT FUS and TDP-43 produced comparable results (Fig. S3).

The effects of FUS and TDP-43 on the dynamics of the RBPs were further evaluated by the cell permeabilization assay. In this assay, permeabilization disrupts the equilibrium of scaffold RBPs between the cytoplasm and granules, causing rapid shrinkage and dissolution of RBPs with liquid properties, even though co-assembled RBPs with solid properties remain within the granules [45]. In neurons forming RNG105 granules, FUS$^{\Delta NLS}$ and TDP-43^{G348C} significantly increased the dissolution and F_m of RNG105 in the granules (Fig. 3A and B), likely due to increased liquidity of RNG105 and/or decreased partitioning of RNG105 within the granules. The F_m of RNG105 was significantly increased even in small-sized granules, showing little correlation with granule size (Fig. 3C). This suggested that even if the expression levels of FUS$^{\Delta NLS}$ and TDP-43^{G348C} were not high enough to form large granules, their concentrations above saturation for phase separation were sufficient to make RNG105 more dynamic. In contrast to RNG105, there was no significant effect of FUS$^{\Delta NLS}$ and TDP-43^{G348C} on the other RBPs (Fig. 3A and B). These results suggested that the accumulation of FUS$^{\Delta NLS}$ and TDP-43^{G348C} in RNA granules increased the fluidity of RNG105 specifically. Also, WT FUS and TDP-43 had similar effects on RNG105 (Figs. S4A and S4B). During these experiments, we noticed relatively rapid dissolution of WT and mutant FUS after permeabilization, suggesting that FUS affected the dynamics of RNG105 without undergoing gelation or solidification (Fig. 3A). These results support the notion that FUS and TDP-43 accumulation in RNA granules specifically increases the fluidity of RNG105.

We further evaluated the effects on endogenous RNG105. Cultured neurons were transfected with FUS$^{\Delta NLS}$ and TDP-43^{G348C} without tags and immunostained for FUS, TDP-43, and endogenous RNG105. We also included immunostaining for other RNA granule components (FMRP and Staufen), processing body (P-body) components (Xrn1 and Dcp2), and ribosomal S6 protein. FUS$^{\Delta NLS}$ and TDP-43^{G348C} formed cytoplasmic granules in the cell body and dendrites, the former containing larger granules with diameters of about 2 μm or greater. Endogenous FMRP was highly overlapped with these granules in both the cell body and dendrites (Fig. 4A–D). In contrast, although endogenous RNG105 accumulated in large granules in the cell body, its subgranular localization pattern was less overlapping and often mutually exclusive with FUS$^{\Delta NLS}$ and TDP-43^{G348C} (Fig. 4A). This pattern resembled previous reports of RNA granules that contain substructures called "core and shell" or "rough and smooth granules", enriched with different components [45, 48]. Related to this exclusive pattern, localization of RNG105 to small granular structures (0.2–0.5 μm in diameter) in dendrites often did not overlap with FUS$^{\Delta NLS}$ or TDP-43^{G348C} granules (Fig. 4B–D). Such granule formation of endogenous RNG105 outside of the FUS$^{\Delta NLS}$ and TDP-43^{G348C} granules was different from the dissolution observed with RNG105-mRFP1. This difference may originate from the increased solubility of RNG105 by mRFP1, which raises the saturation concentration of RNG105 for phase separation.

In contrast to RNG105, endogenous Staufen and S6, like FMRP, were highly concentrated in FUS$^{\Delta NLS}$ and TDP-43^{G348C} granules, except for P-body proteins Xrn1 and Dcp2 (Fig. 4D). Consistent with these results, even in the absence of FUS$^{\Delta NLS}$ or TDP-43^{G348C} overexpression, endogenous FUS and TDP-43 colocalized less with endogenous RNG105 than with endogenous FMRP and Staufen (Fig. 4E). Overall, these results showed that, despite the difference in solubility, endogenous RNG105 behaved similarly to RNG105-mRFP1, being excluded from FUS$^{\Delta NLS}$- and TDP-43^{G348C}-enriched granules in dendrites.

We conducted further investigations into the colocalization of endogenous RNG105 with other endogenous granule proteins and its response to FUS$^{\Delta NLS}$ and TDP-43^{G348C} overexpression. RNG105 colocalized with FMRP and Staufen in dendritic granules without FUS$^{\Delta NLS}$ or TDP-43^{G348C} overexpression (Fig. S5A). This colocalization, especially with Staufen, was reduced by FUS$^{\Delta NLS}$ and TDP-43^{G348C} expression, but not by other proteins such as FMRP, Stau1, or Pum2 (Figs. S5A–S5C). This reduced colocalization may be due to the localization equilibrium of FMRP and Staufen being biased towards FUS$^{\Delta NLS}$ and TDP-43^{G348C} granules over RNG105 granules and the cytoplasm. Alternatively, it may be due to the diffuse localization pattern of RNG105 in FMRP and Staufen granules (Fig. S5A). Colocalization of RNG105 with other proteins, Xrn1, Dcp2, and S6, was lower than with FMRP and Staufen, and was mostly unaffected by FUS$^{\Delta NLS}$ or TDP-43^{G348C} expression, except for the colocalization with Xrn1 (Figs. S5D–S5G). This exception could be related to the fact that Xrn1 is localized not only in P-bodies but also in different assemblies in neurons [49]. These results indicated that the colocalization of endogenous RNG105 with RNA granule RBPs was specifically affected by FUS$^{\Delta NLS}$ and TDP-43^{G348C} overexpression. In contrast to overexpression, knockdown of FUS or TDP-43 did not affect the colocalization of endogenous RNG105 with FMRP or Staufen (Fig. S6), suggesting that the low cytoplasmic concentration of endogenous FUS and TDP-43 (Figs. S1A and S1B, arrows) may not significantly bias the localization equilibrium of RNG105 and other RNA granule RBPs in the cytoplasm.

In conclusion, we observed significant effects of FUS and TDP-43 on the dynamics of RNG105 and FMRP within RNA granules, resulting in increased mobility of RNG105 and its dissociation from the granules. Since RNG105 plays a crucial role in mRNA transport in dendrites and is essential for synaptic plasticity and long-term memory formation [32,50], changes in its dynamics within RNA granules may affect mRNA localization and local translation in/near the granules. Therefore, we proceeded to investigate the effects of
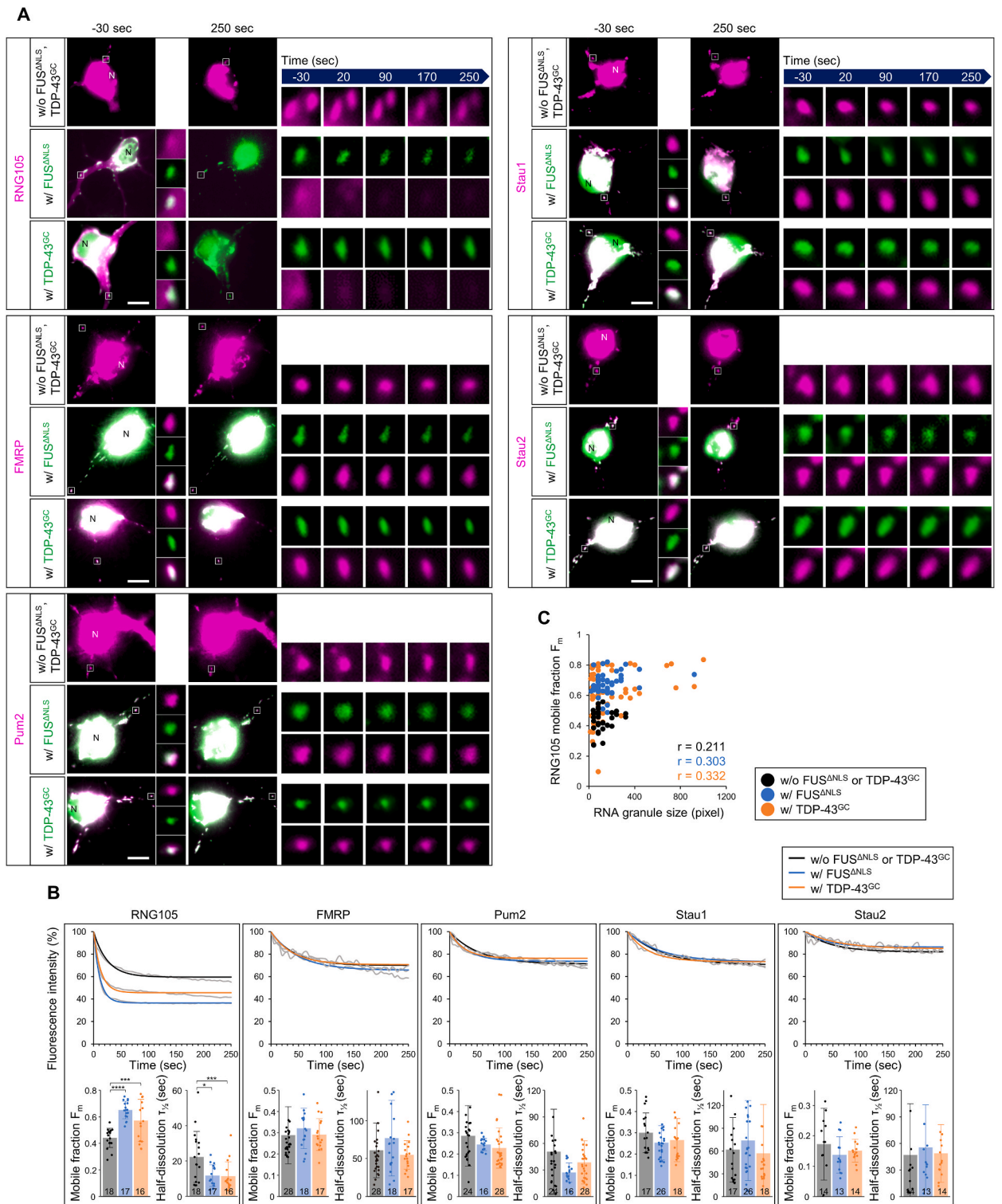
(caption on next page)

Fig. 3. FUS$^{\Delta NLS}$ and TDP-43^{G348C} accumulation increases the fluidity of RNG105 in RNA granules. (A) Representative time-lapse images of mRFP1-tagged RBPs in neurons with and without expression of GFP-tagged FUS$^{\Delta NLS}$ or TDP-43^{GC} in cell permeabilization analysis. Neurons became permeable by digitonin shortly after time 0. The boxed areas containing dendritic RNA granules are magnified in the insets and the right panels. Shrinkage and dissolution of RNG105 granules were accelerated by FUS$^{\Delta NLS}$ and TDP-43^{GC} in cell bodies and dendrites. *N*, nuclei. Scale bars, 10 μm. **(B)** Top, representative time-course changes in fluorescence intensity of RBPs in dendritic granules, and fitted curves with exponential equations. The gray lines show the measured values. The difference between the samples with and without FUS/TDP-43 appears smaller in the graphs than in the images because the extracellular background fluorescence intensity, which changes after cell permeation due to the efflux of fluorescent proteins, was not subtracted as the subtraction would affect the fitting with the exponential equation. Bottom, the mobile fraction (F_m) and halftime of dissolution ($\tau_{1/2}$) extracted from the fitted equations. **(C)** Relationship between granule size and F_m of RNG105 within the granules. Pearson's correlation coefficients (r) are indicated. In B, the data are represented by scatter plots of the individual values, stated as the mean ± S.D. The number of dendrites analyzed from 4 independent cultures is shown in the graph. *p < 0.05, ***p < 0.005, ****p < 0.001, Tukey-Kramer test after one-way ANOVA. See also Fig. S4.

FUS and TDP-43 on mRNA localization and local translation in RNG105-localizing RNA granules in dendrites.

## 2.2. FUS and TDP-43 accumulation reduces the amount of mRNA and translation in dendritic RNA granules

First, the localization of mRNAs in RNA granules was examined by fluorescence in situ hybridization (FISH) using a poly (dT) probe. In the absence of FUS$^{\Delta NLS}$ or TDP-43^{G348C} expression, mRNAs were accumulated in RNA granules where RNG105 was concentrated (Fig. 5A). However, FUS$^{\Delta NLS}$ and TDP-43^{G348C}-enriched granules reduced the concentration of mRNAs, which may be due to reduced recruitment and/or stability of mRNAs in the granules (Fig. 5A and B). Comparable results were obtained in experiments with WT FUS and TDP-43 (Fig. S7A). Furthermore, experiments without tags, such as untagged RNG105, FUS$^{\Delta NLS}$, and TDP-43^{G348C}, also yielded similar results (Figs. S7C and S7D). It should be noted that, although RNG105 without mRFP1 tag formed granules outside of FUS$^{\Delta NLS}$ and TDP-43^{G348C} granules like endogenous RNG105, those RNG105 granules were smaller and had less-defined borders, and RNG105 was more diffuse throughout the cytoplasm compared with the absence of FUS$^{\Delta NLS}$ or TDP-43^{G348C} expression (Fig. S7C). These results indicate that the accumulation of FUS and TDP-43 in RNA granules reduces the amount of both RNG105 and mRNAs within the granules.

Next, translation activity in/near RNA granules was measured using the SunTag system, which detects newly synthesized polypeptides by scFv-GFP binding to SunTag polypeptides at the time and place of translation [51]. The mRNA encoding the SunTag polypeptide was fused to the *Arc* 3'UTR to be recruited into RNA granules for local translation in/near the granules [51]. In the absence of FUS$^{\Delta NLS}$ or TDP-43^{G348C} expression, SunTag mRNA was indeed enriched in RNG105-localizing granules (Fig. 5C). Correspondingly, the SunTag translation signal was concentrated around the granules (Fig. 5F). Without SunTag mRNA, no such condensation was observed (Fig. 5H), confirming that the signal indicated local translation around the granules. As translating polysomes are reportedly observed by electron microscopy to attach around purified neuronal RNA granules, it appears that the translation of cargo mRNAs may occur locally in the vicinity of the granules [52].

However, when FUS$^{\Delta NLS}$ and TDP-43^{G348C} were accumulated in RNA granules, SunTag mRNA was lost from the granule region (Fig. 5C–E), and the SunTag translation signal was reduced and eliminated from the granules (Fig. 5F and G). This effect was also observed in experiments using WT FUS and TDP-43 (Fig. S7B). Furthermore, experiments with untagged RNG105, FUS$^{\Delta NLS}$, and TDP-43^{G348C} also yielded similar results (Figs. S7E and S7F). During the experiments with the untagged proteins, we noted that when FUS$^{\Delta NLS}$ and TDP-43^{G348C} were expressed, SunTag signals were scattered throughout the cytoplasm, overlapping with the small and indistinct RNG105 granules outside FUS$^{\Delta NLS}$ and TDP-43^{G348C} granules (Fig. S7E). These results demonstrated that the accumulation of FUS and TDP-43 in RNA granules reduced translation in/near the granules, scattering the translation sites with RNG105. This was in line with the reduced mRNA recruitment into the granules, and may be due in part to reduced translation efficiency in the granules as suggested by translational co-repression by TDP-43 and FMRP [53], and reduced mRNA stability in the granules as suggested by mRNA destabilization by TDP-43 deposition [54,55]. Furthermore, these results raised the question of whether the reduction in mRNAs and translation in/near the granules was mediated by the dissociation of RNG105 from the granules.

2.3. RNG105 RBD1 is responsible for the FUS- and TDP-43-induced increases in RNG105 dynamics and dissociation from RNA granules

To address this issue, we identified the domains of RNG105 responsible for the dissociation, focusing on the RNA granule assembly domains RBD1 and RBD2, and IDRs with low sequence complexity such as Glu (E)-rich and Gln (Q)-rich domains [56] (Fig. 6A). We generated several mutants, including RNG105-ΔRBD1 with RBD1 deleted, RNG105-Pum2RBD and RNG105-Stau1RBD with RBD1 replaced with the RBDs of Pum2 and Stau1, respectively (Fig. 6A). For RNG105-Stau1RBD, we used RBD3 and RBD4 of Stau1, which are required for RNA binding [57,58]. We also generated mutants with FUS RGG/RG motifs replacing RNG105 RBD2 (RGG/RG-rich domain) and mutants with E-rich and Q-rich domains deleted (Fig. S8A). Co-localization analysis revealed that the RBD2 substituted mutants and IDR deletion mutants either lost their ability to form RNA granules or did not alter the FUS$^{\Delta NLS}$- and TDP-43^{G348C}-induced dissociation (Figs. S8A and S8B). In contrast, RNG105-ΔRBD1 reduced dissociation, suggesting that RBD1 was the FUS- and TDP-43-sensitive domain (Fig. S9). However, this reduced dissociation was restricted to large, dense granules in the cell body and proximal dendrites (Fig. S9), and not observed in dendrites (Fig. 6A and B), suggesting a weakened affinity of RNG105-ΔRBD1 for RNA granules. Replacement of RBD1 with Pum2 and Stau1 RBDs terminated the FUS$^{\Delta NLS}$- and TDP-43^{G348C}-induced dissociation from RNA granules, even in distal dendrites (Fig. 6A and B).

A

B

C

r = 0.301

r = 0.847

r = 0.410

r = 0.750

D

E

RNG105
FMRP
Staufen
Xrn1
Dcp2
S6
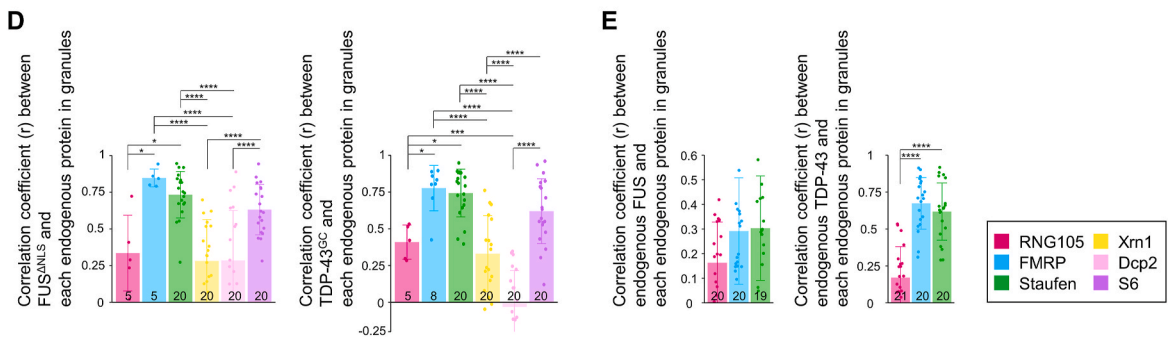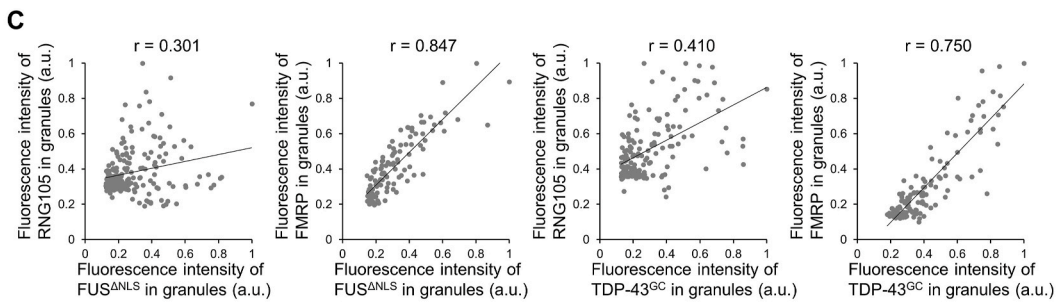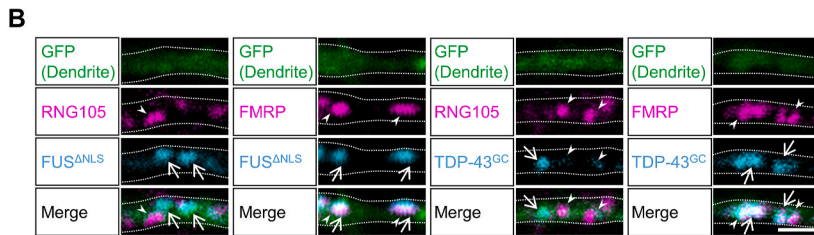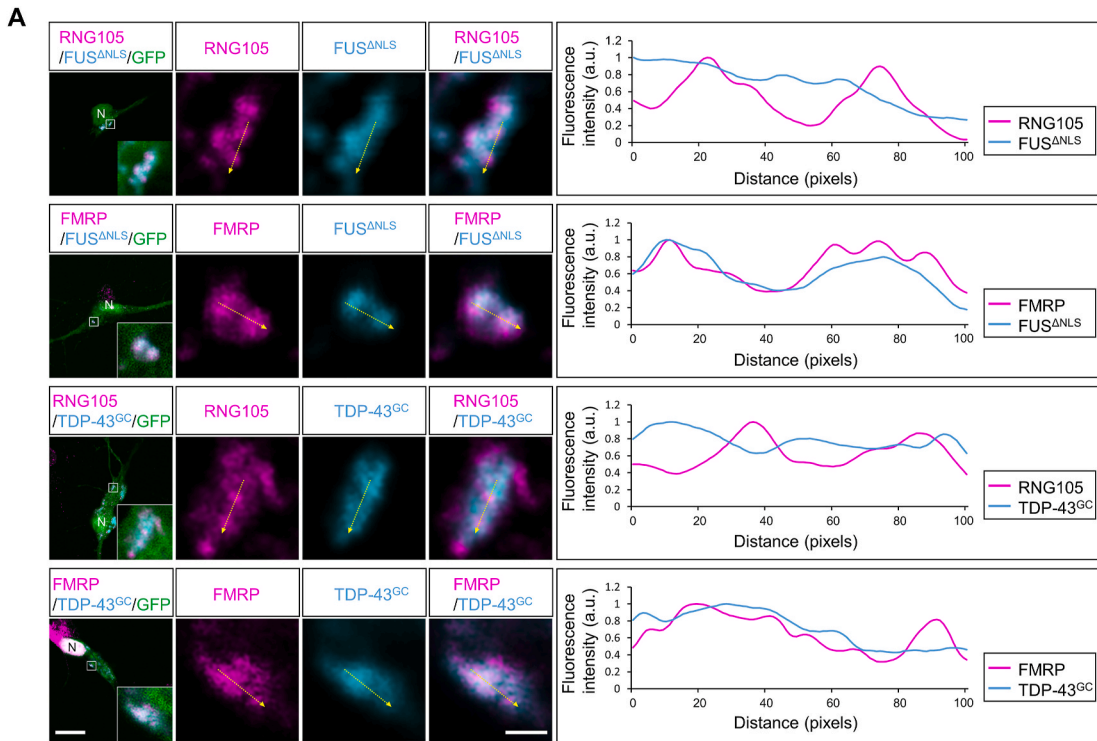
(caption on next page)

Fig. 4. Limited accumulation of endogenous RNG105 into FUS and TDP-43-enriched granules. (A and B) Cultured neurons transfected with untagged FUS$^{\Delta NLS}$ or TDP-43^{GC} were immunostained for FUS, TDP-43, and endogenous RNG105 and FMRP in/near the cell body (A) and dendrites (B). The neurons were co-transfected with GFP to visualize the morphology of neurons. In A, the boxed areas containing RNA granules are magnified in the insets and the right panels. The immunofluorescence intensity of the RBPs within the granules was measured along the dotted arrows to analyze their subgranular localization pattern and is shown in the rightmost panels. *N*, nuclei. Scale bars, 10 μm (left) and 1 μm (right). In B, arrowheads indicate dendritic granules where endogenous RNG105 and FMRP accumulated. Arrows indicate dendritic granules formed by FUS$^{\Delta NLS}$ and TDP-43^{GC}. Scale bar, 1 μm. **(C)** Representative graphs showing the relationship between the fluorescence intensity of FUS$^{\Delta NLS}$ or TDP-43^{GC} and that of endogenous RNG105 or FMRP in dendritic RNA granules in a single neuron. Regression lines and Pearson's correlation coefficients are indicated. **(D)** Similar experiments as in B and C were performed for endogenous RNG105, FMRP, Staufen, Xrn1, Dcp2, and ribosomal S6, and Pearson's correlation coefficients were statistically analyzed. **(E)** Untransfected cultured neurons were immunostained for RBPs and the colocalization of endogenous RNG105, FMRP, and Staufen with endogenous FUS and TDP-43 in dendritic granules was analyzed as in D. The data are represented by scatter plots of the individual values, stated as the mean ± S.D. The number of neurons analyzed from two independent cultures is shown in the graph. *p < 0.05, ***p < 0.005, ****p < 0.001, Tukey-Kramer test after one-way ANOVA. See also Figs. S5 and S6.

Given such alterations by replacement of RNG105 RBD1, the dynamics of RNG105-Pum2RBD and RNG105-Stau1RBD were analyzed by FRAP in dendritic RNA granules. In the absence of FUS$^{\Delta NLS}$ or TDP-43^{G348C}, these RNG105 mutants had much lower F_m and much longer $t_{1/2}$ than WT RNG105, indicating their reduced dynamics in RNA granules (Fig. 6C and S10). When co-expressed with FUS$^{\Delta NLS}$ and TDP-43^{G348C}, the F_m of WT RNG105 in the granules increased significantly, whereas the F_m of RNG105-Pum2RBD and RNG105-Stau1RBD showed no increase (Fig. 6C and S10). Taken together, RBD1 of RNG105 was responsible for the high dynamics of RNG105 in RNA granules even in the absence of FUS$^{\Delta NLS}$ or TDP-43^{G348C}, and for the FUS$^{\Delta NLS}$- and TDP-43^{G348C}-induced increased dynamics and dissociation of RNG105 from RNA granules.

The next question was whether RNG105 RBD1 was sufficient to be sensitive to FUS$^{\Delta NLS}$ and TDP-43^{G348C}. To address this, we replaced the RBDs of RNA granule RBPs such as Pum2, FMRP, and Stau1 with the RBD1 of RNG105. Replacing the Pum2 RBD with RNG105 RBD1 abolished the ability to form RNA granules, making it impossible to analyze the sensitivity of this mutant to FUS$^{\Delta NLS}$ and TDP-43^{G348C} (Fig. S11A). Replacing the FMRP RBDs (KH0, KH1, and KH2) with RNG105 RBD1 did not alter sensitivity to FUS$^{\Delta NLS}$ or TDP-43^{G348C} (Figs. S11B and S11C). In the case of Stau1, combinations of the four RBDs were replaced with RNG105 RBD1, generating six Stau1 RBD-substituted mutants (Stau1-105RBD1-1 to Stau1-105RBD1-6) (Fig. 7A and S12A). Among these mutants, those carrying Stau1 RBD2 (Stau1-105RBD1-3 to Stau1-105RBD1-6) were not sensitive to FUS$^{\Delta NLS}$ or TDP-43^{G348C} (Figs. S12A and S12B). However, the Stau1 mutants in which Stau1 RBD2-RBD4 were replaced (Stau1-105RBD1-1) showed sensitivity to FUS$^{\Delta NLS}$ and TDP-43^{G348C} (Fig. 7A and B). Removal of RNG105 RBD1 from this mutant abolished RNA granule-forming ability, confirming that RNG105 RBD1 was required for FUS$^{\Delta NLS}$- and TDP-43^{G348C}-sensitive RNA granule localization (Fig. 7A, Stau1-ΔRBD-1). Similar sensitivity to FUS$^{\Delta NLS}$ and TDP-43^{G348C} was also observed in Stau1-105RBD1-2 in which all Stau1 RBDs were replaced by RNG105 RBD1 (Figs. S12A and S12B).

To gain more insights into the dynamics of Stau1-105RBD1-1 in RNA granules, we performed FRAP analysis. The mobility of Stau1-105RBD1-1 in RNA granules in the absence of FUS$^{\Delta NLS}$ or TDP-43^{G348C} was very low, as shown by the lower F_m than WT Stau1 (Fig. 7C and S13). However, the F_m of Stau1-105RBD1-1 was markedly elevated by expression of FUS$^{\Delta NLS}$ and TDP-43^{G348C}, resulting in a much higher F_m than WT Stau1 (Fig. 7C and S13). Taken together, these results suggest that RBD1 of RNG105 confers sensitivity to FUS$^{\Delta NLS}$ and TDP-43^{G348C} in specific combinations with other domains. This may mean that domains other than RBD1 must have the ability to associate with RNA granules without tightly binding to them.

In addition to RNG105's domain, we identified the domains of FUS$^{\Delta NLS}$ and TDP-43^{G348C} that are responsible for RNG105 dissociation. Each domain of FUS$^{\Delta NLS}$ and TDP-43^{G348C} was systematically deleted (Fig. S14A), and these mutants were expressed in neurons as GFP-tagged proteins. Despite differences in the density of dendritic granules, all mutants formed granules in dendrites, where RNA granule-constituting proteins co-localized (Fig. S14B). These results suggested that FUS$^{\Delta NLS}$ and TDP-43^{G348C} interact with RNA granule constituents through multiple domains to condense into RNA granules. When co-expressed with RNG105-mRFP1, all of the deletion mutants caused RNG105 to dissociate from granules (Figs. S14C and S14D). Thus, RNG105 dissociation was not mediated by specific domains of FUS$^{\Delta NLS}$ or TDP-43^{G348C}, suggesting that neither their RNA-binding capacity nor specific protein-protein interactions were required for dissociating RNG105. Since RBD1 of RNG105 participates in RNA granule assembly, i.e., co-phase separation with RNA granule components [45,56], these results suggest that phase separation of FUS$^{\Delta NLS}$ and TDP-43^{G348C} with RNA granule components biased the equilibrium of co-phase separation of RNG105 towards dissociation, although the underlying mechanism for this bias remains unknown.

2.4. Non-dissociable RNG105 mutants suppress the reduction of mRNA and translation levels in RNA granules caused by FUS and TDP-43

To investigate whether FUS- and TDP-43-induced reduction in mRNA and translation levels in RNA granules were mediated by the dissociation of RNG105 from the granules, we assessed whether the non-dissociable RNG105-Pum2RBD and RNG105-Stau1RBD suppress the effects of FUS and TDP-43. First, mRNA localization in RNA granules was quantified by FISH with poly (dT). In neurons expressing WT RNG105, the accumulation of FUS$^{\Delta NLS}$ and TDP-43^{G348C} reduced the amount of mRNA in RNA granules (Fig. 8A, D, and 8E). However, the reduction of mRNA levels by FUS$^{\Delta NLS}$ and TDP-43^{G348C} was significantly suppressed by RNG105-Pum2RBD, as determined by the interaction effect in the two-way ANOVA (Fig. 8B and D). Essentially the same results were obtained for RNG105-Stau1RBD (Fig. 8C and E). We noted that there was still a reduction in mRNA levels by TDP-43^{G348C} in both cases (Fig. 8D and E), which could be attributed to the effects of TDP-43^{G348C} on endogenous RNA granule components. These results suggest that FUS$^{\Delta NLS}$-

and TDP-43[G348C]-induced reductions in the mRNA level in RNA granules are due to the dissociation of RNG105 from the granules.

These results raised the question of whether the recruitment of mRNAs into RNA granules by RNG105 was mediated by RBD1 alone or if other domains of RNG105 were also involved. To answer this, we expressed RNG105 domain deletion mutants in RNG105 knockout neurons [50] and performed FISH with poly (dT). The deletion of another RBD, RBD2, abolished the ability to form RNA granules [56], making it impossible to evaluate mRNA recruitment to RNA granules through this domain. Since RNA recruitment to granules has been reported to be affected by the condensation state of RNA-containing granules, regardless of the RNA-binding specificity of RBDs [59,60], we also tested the IDRs of RNG105, namely E-rich and Q-rich domains. RNG105ΔQ was unable to
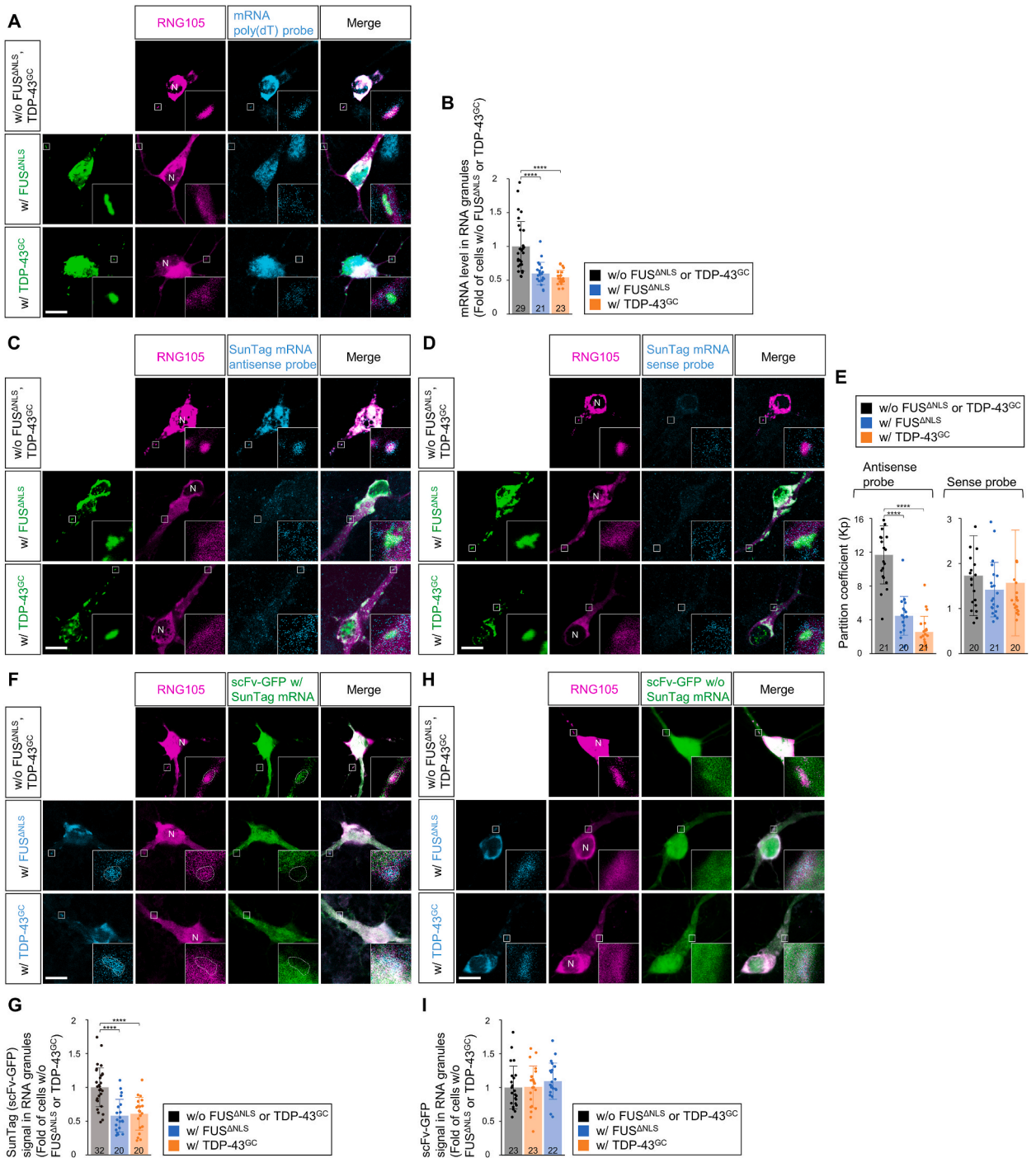
(caption on next page)

Fig. 5. Accumulation of FUS$^{\Delta NLS}$ and TDP-43^{G348C} reduces the amount of mRNA and translation in/near dendritic RNA granules. (A) Neurons expressing RNG105-mRFP1 with and without expression of GFP-tagged FUS$^{\Delta NLS}$ or TDP-43^{GC} were stained by *in situ* hybridization with poly (dT) for mRNA detection. The boxed areas containing dendritic RNA granules are magnified in the insets. *N*, nuclei. **(B)** The mRNA levels in the dendritic RNA granules were measured and normalized to those in the dendrites of neighboring untransfected neurons. **(C and D)** Neurons expressing RNG105-mRFP1 and SunTag mRNA with and without expression of GFP-tagged FUS$^{\Delta NLS}$ or TDP-43^{GC} were *in situ* hybridized with SunTag antisense (C) or sense (D) probes. **(E)** Accumulation of SunTag mRNA in dendritic RNA granules was quantified by calculating the granule/cytoplasm partition coefficient. **(F)** Neurons expressing RNG105-mRFP1 with and without Sirius-tagged FUS$^{\Delta NLS}$ or TDP-43^{GC} were co-transfected with SunTag mRNA and scFv-GFP to detect nascent SunTag polypeptides. **(G)** The SunTag signal (scFv-GFP accumulation to SunTag polypeptides) in dendritic RNA granules was measured and normalized by min-max normalization in each neuron. **(H)** Control experiments for F without SunTag mRNA. Note that the neurons showed no accumulation/removal of scFv-GFP in/from the granules. **(I)** The scFv-GFP signal in dendritic RNA granules was analyzed as in G. Scale bars, 10 μm. The data are represented by scatter plots of the individual values, stated as the mean ± S.D. The number of neurons analyzed from three independent cultures is shown in the graph. ****p < 0.001, Tukey-Kramer test after one-way ANOVA. See also Fig. S7.

form dendritic RNA granules, whereas RNG105ΔE did (Fig. S8A). However, mRNA accumulation in RNG105ΔE granules was much less than in WT RNG105 granules (Fig. S15). These results indicated that the E-rich domain of RNG105 was required to recruit higher amounts of mRNA to the granules, suggesting that RNG105 recruits mRNAs into the granules through IDRs, at least through the E-rich domain, as well as RBD1 and RBD2 that are required for RNA granule assembly.

Next, translation activity in/near RNA granules was measured using SunTag. In neurons expressing WT RNG105, accumulation of FUS$^{\Delta NLS}$ and TDP-43^{G348C} in RNA granules significantly reduced the SunTag signal in the granules (Fig. 8F, I, and 8J). However, this reduction by FUS$^{\Delta NLS}$ and TDP-43^{G348C} was suppressed by RNG105-Pum2RBD (Fig. 8G and I). Notably, in neurons expressing RNG105-Stau1RBD, the SunTag signal in the granules was lower than that in WT RNG105 granules in the absence of FUS$^{\Delta NLS}$ or TDP-43^{G348C} expression (Fig. 8H and J). Nevertheless, RNG105-Stau1RBD suppressed the FUS$^{\Delta NLS}$- and TDP-43^{G348C}-induced decrease in the SunTag signal in the granules (Fig. 8H and J), similar to RNG105-Pum2RBD. Taken together, the non-dissociable RNG105 mutants retained mRNA and translation levels in RNA granules when FUS$^{\Delta NLS}$ and TDP-43^{G348C} accumulated in the granules, which suggested that FUS$^{\Delta NLS}$- and TDP-43^{G348C}-induced dissociation of RNG105 from the granules mediated the reduction of mRNA and translation levels in/near the granules.

2.5. The non-dissociable RNG105 mutations attenuate dendritic spine loss caused by the combination of FUS/TDP-43 and WT RNG105

Next, we investigated the effects of the non-dissociable RNG105 mutants on dendritic spine formation affected by FUS$^{\Delta NLS}$ and TDP-43^{G348C}. To visualize neuron morphology, including dendritic spines, we co-transfected neurons with GFP together with untagged RBPs. Expression of FUS$^{\Delta NLS}$ alone reduced the spine density and abundance of mature mushroom spines in dendrites, as observed with WT FUS (Fig. S16A). Co-expression of WT RNG105 maintained or even intensified the FUS-induced spine reduction (Fig. S16C). However, these spine reductions caused by the combination of FUS$^{\Delta NLS}$ and WT RNG105 were attenuated by replacing RNG105 RBD1 with Pum2RBD (Fig. 9A and C). This attenuation may not be solely attributed to Pum2RBD, as the expression of Pum2 rather abolished spine formation (Fig. S16E). In neurons expressing RNG105-Stau1RBD, dendritic spine density was lower than in neurons expressing WT RNG105 in the absence of FUS$^{\Delta NLS}$ (Fig. 9A and D). This spine loss may be related to the decreased translation by RNG105-Stau1RBD in/near the granules in the absence of FUS$^{\Delta NLS}$ (Fig. 8J). Because similar spine loss was observed in Stau1-expressing neurons (Fig. S16G), Stau1RBD may be responsible for those adverse effects. Nevertheless, the combined effect of FUS$^{\Delta NLS}$ and RNG105-Stau1RBD on spine formation was relatively neutral compared with the severe effect of the combination of FUS$^{\Delta NLS}$ and WT RNG105 (Fig. 9D). Therefore, we concluded that the toxicity caused by the combination of FUS$^{\Delta NLS}$ and WT RNG105 was reduced by the substitution of RNG105 RBD1.

Similar to FUS, a single expression of TDP-43^{G348C} in neurons reduced dendritic spine formation, as did WT TDP-43 (Fig. S16B). Co-expression of WT RNG105 maintained or even enhanced the TDP-43-induced spine reduction, leading to cell death within 3 days after transfection (Fig. S16D). However, this spine loss and cell death by the combination of TDP-43^{G348C} and WT RNG105 was ameliorated by replacing RNG105 RBD1 with Pum2RBD (Fig. 9B and E). Essentially the same results were obtained by replacing RNG105 RBD1 with Stau1RBD, although it should be noted that Stau1RBD may adversely affect spine formation (Fig. 9B and F). These results suggest that the toxicity caused by the combination of TDP-43^{G348C} and WT RNG105 is reduced by the substitution of RNG105 RBD1, as was the case of FUS$^{\Delta NLS}$.

Given these results, we tested whether RNG105 knockdown would conversely alleviate the effects of FUS and TDP-43 (Figs. S17A–S17D). Knockdown of RNG105 itself reduced spine density and abundance of mature mushroom spines in dendrites (Figs. S17C and S17D), consistent with previous reports [32,50]. Therefore, it was challenging to evaluate the effects of FUS and TDP-43 in the absence of RNG105. Nevertheless, although RNG105 knockdown and FUS$^{\Delta NLS}$/TDP-43^{G348C} expression each independently affected spine formation, there was no synergistic effect (Figs. S17C and S17D), which was in contrast to the combination of FUS/TDP-43 and WT RNG105 expression that caused cell death in the case of TDP-43 (Fig. 9C–F, S16C, and S16D). These findings may support the notion that RNG105 has adverse effects in combination with FUS and TDP-43.

In summary, the non-dissociable RNG105 mutations suppressed the loss of mRNAs and translation in RNA granules and further suppressed the loss of synapse formation, caused by the combination of FUS/TDP-43 and WT RNG105. These results suggest that increased fluidity and dissociation of RNG105 from RNA granules mediated the FUS$^{\Delta NLS}$- and TDP-43^{G348C}-induced defects in local translation and synapse formation in dendrites.
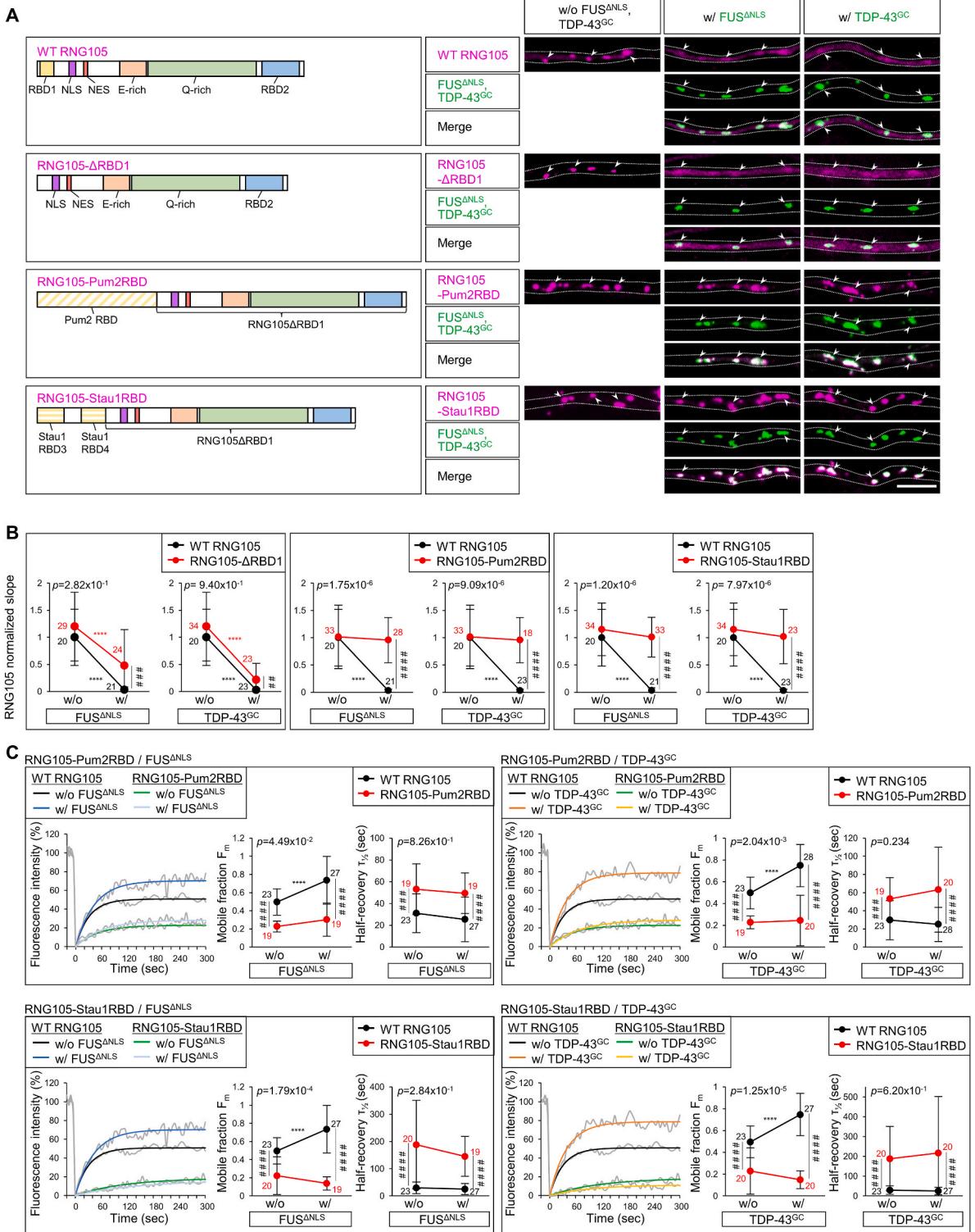
Fig. 6. RBD1 of RNG105 is responsible for the FUS$^{\Delta NLS}$- and TDP-43^{G348C}-caused increased dynamics of RNG105 in RNA granules. (A) Left panels, schematic of wild-type (WT) and mutant RNG105. RBD1 of RNG105 was deleted or replaced with Pum2 RBD or Stau1 RBDs. RBD, RNA-binding domain; NLS, nuclear localization signal; NES, nuclear export signal; E-rich, glutamic acid-rich domain; Q-rich, glutamine-rich domain. Right panels, localization of mRFP1-tagged WT and mutant RNG105 to RNA granules in dendrites, and the effect of expression of GFP-tagged FUS$^{\Delta NLS}$ and TDP-43^{GC} on that localization. Arrowheads indicate representative RNA granules in the dendrites. The dotted lines outline the dendrites. Scale bar, 5 μm. **(B)** Degree of accumulation of WT and mutant RNG105 in dendritic RNA granules as assessed by the slope of RNG105

fluorescence in single granules. **(C)** FRAP analysis was performed on mRFP1-tagged WT and mutant RNG105 in neurons with and without expression of GFP-tagged FUS$^{\Delta NLS}$ or TDP-43^{GC}. Left columns, representative FRAP curves for WT and mutant RNG105 in dendritic RNA granules. Right columns, the mobile fraction (F_m) and halftime of recovery ($\tau_{\frac{1}{2}}$). The data are stated as the mean ± S.D. The number of granules analyzed from 3 (B) and 4 (C) independent cultures is shown in the graph. The p-values for the interaction effect in two-way ANOVA are indicated. ****p < 0.001, ##p < 0.01, ###p < 0.005, ####p < 0.001, post-hoc Student's t-test after two-way ANOVA. See also Figs. S8–S10.
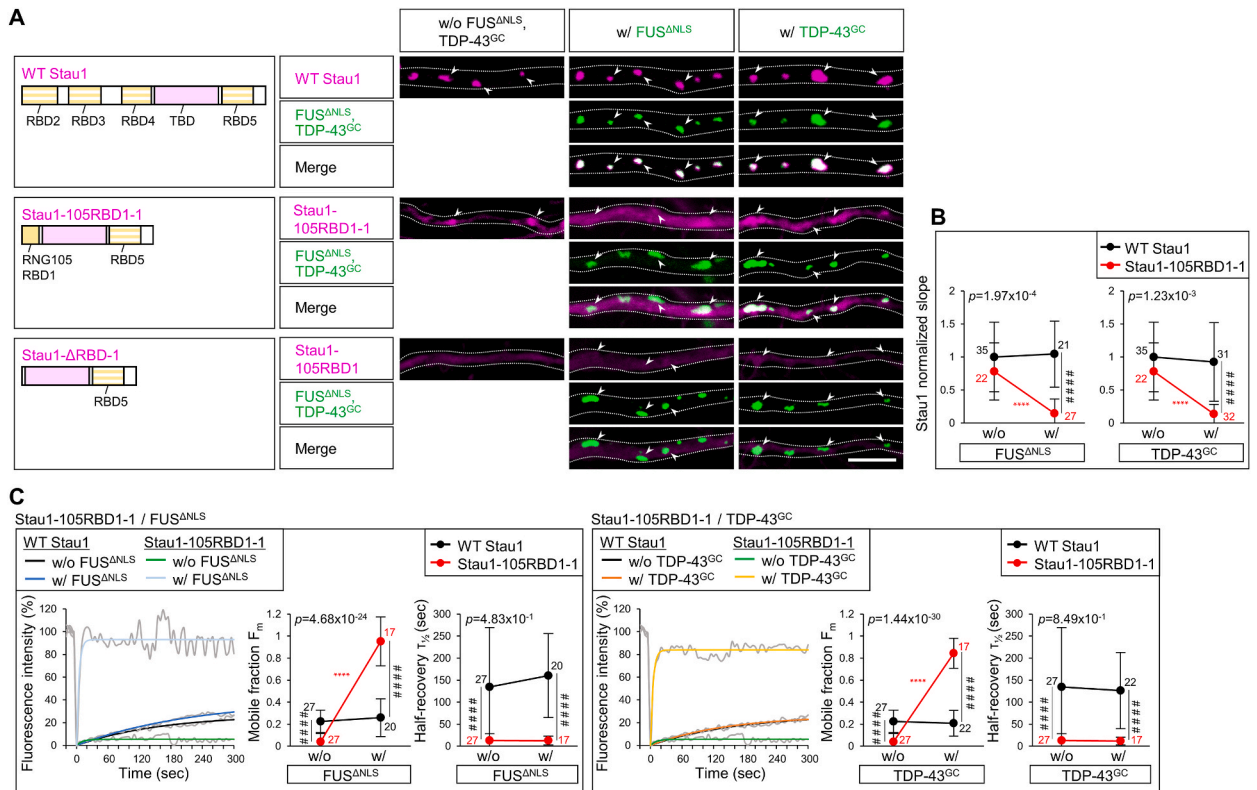

Fig. 7. Replacing Stau1 RBDs with RNG105 RBD1 makes Stau1's RNA granule localization sensitive to FUS$^{\Delta NLS}$ and TDP-43^{G348C}. (A) Left panels, schematic of WT and mutant Stau1. In the mutants, Stau1 RBD2-RBD4 was replaced by RNG105 RBD1 or deleted. Right panels, localization of mRFP1-tagged WT and mutant Stau1 to RNA granules in dendrites, and the effect of expression of GFP-tagged FUS$^{\Delta NLS}$ and TDP-43^{GC} on that localization. Arrowheads indicate representative RNA granules in the dendrites. The dotted lines outline the dendrites. Scale bar, 5 μm. **(B)** Degree of accumulation of WT and mutant Stau1 in dendritic RNA granules. **(C)** FRAP analysis was performed on mRFP1-tagged WT and mutant Stau1 in neurons with and without expression of GFP-tagged FUS$^{\Delta NLS}$ or TDP-43^{GC}. Left columns, representative FRAP curves for WT and mutant Stau1 in dendritic RNA granules, and fitted curves with exponential equations. Right columns, the mobile fraction (F_m) and halftime of recovery ($\tau_{\frac{1}{2}}$). The data are stated as the mean ± S.D. The number of granules analyzed from 3 (B) and 4 (C) independent cultures is shown in the graph. The p-values for the interaction effect in two-way ANOVA are indicated. ****p < 0.001, ####p < 0.001, post-hoc Student's t-test after two-way ANOVA. See also Figs. S11–S14.

3. Discussion

We showed here that the accumulation of FUS and TDP-43 in dendritic RNA granules increased the RNG105 dynamics and dissociation from the granules, leading to a reduction in the amount and local translation of mRNA around the granules. However, non-dissociable RNG105 suppressed this reduction, as well as FUS- and TDP-43-induced synaptic loss and neuronal cell death, suggesting that RNG105 dissociation from dendritic RNA granules mediates the loss of mRNA and local translation in/near the granules and synapse impairment (Graphical abstract). Thus, RNG105 may play a critical role in localizing mRNAs to RNA granules and facilitating translation in/near the granules. This role is reminiscent of a report showing that RNG105 accumulation in RNA granules dose-dependently suppresses FUS-induced translational repression [45], and is consistent with the RNG105 knockout phenotype in mice, including defects in dendritic mRNA transport, synaptic potentiation, and long-term memory formation [32].

Dissociated RNG105 can scatter small granules with indistinct boundaries where translation occurs outside the FUS- and TDP-43-accumulating granules, potentially compromising the spatiotemporal regulation of local translation. Loss of spatiotemporal regulation can reduce synaptic stimulation-dependent local translation near stimulated spines, which may attenuate translation-dependent plastic changes of the stimulated spines and may be associated with cognitive impairment [30,31].
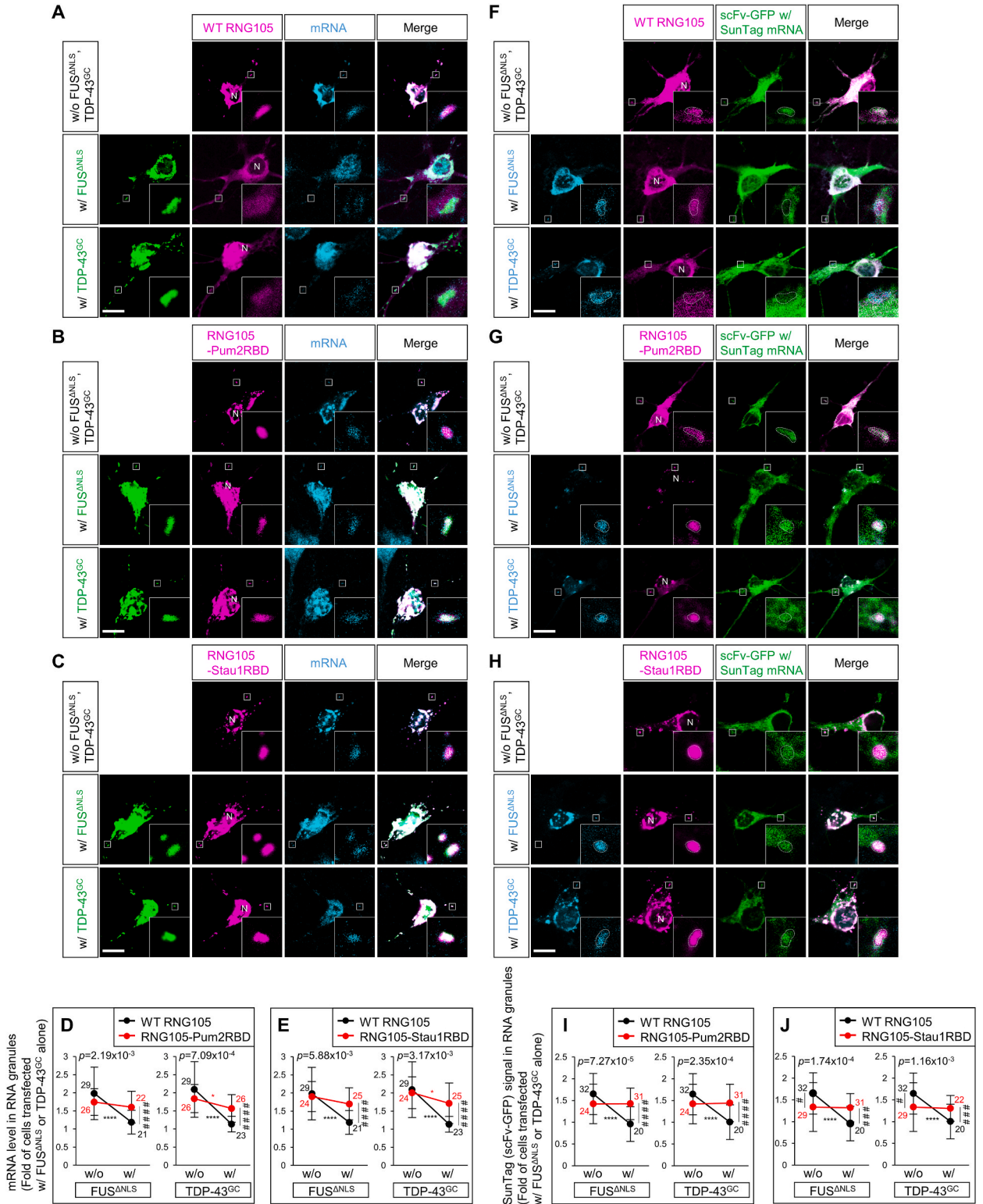
(caption on next page)

Fig. 8. The RBD1-substituted mutants of RNG105 suppress the FUS$^{\Delta NLS}$- and TDP-43^{G348C}-caused decrease in mRNA and translation levels in/near dendritic granules. (A–C) Neurons expressing mRFP1-tagged WT and RBD1-substituted mutants of RNG105, with and without expression of GFP-tagged FUS$^{\Delta NLS}$ or TDP-43^{GC}, were stained by *in situ* hybridization with poly (dT) for mRNA detection. The boxed areas containing dendritic RNA granules are magnified in the insets. *N*, nuclei. **(D and E)** The mRNA levels in dendritic RNA granules were measured and normalized to those in the dendrites of neighboring untransfected neurons. **(F–H)** Neurons expressing WT and mutant RNG105 with and without expression of Sirius-tagged FUS$^{\Delta NLS}$ or TDP-43^{GC} were co-transfected with SunTag for the detection of nascent polypeptides. **(I and J)** The SunTag signal in the dendritic RNA granules was measured and normalized by min-max normalization in each neuron. Scale bars, 10 μm. The data are stated as the mean ± S.D. The number of neurons analyzed from three independent cultures is shown in the graph. The p-values for the interaction effect in two-way ANOVA are indicated. *p < 0.05, ****p < 0.001, #p < 0.05, ###p < 0.005, ####p < 0.001, post-hoc Student's t-test after two-way ANOVA. See also Fig. S15.
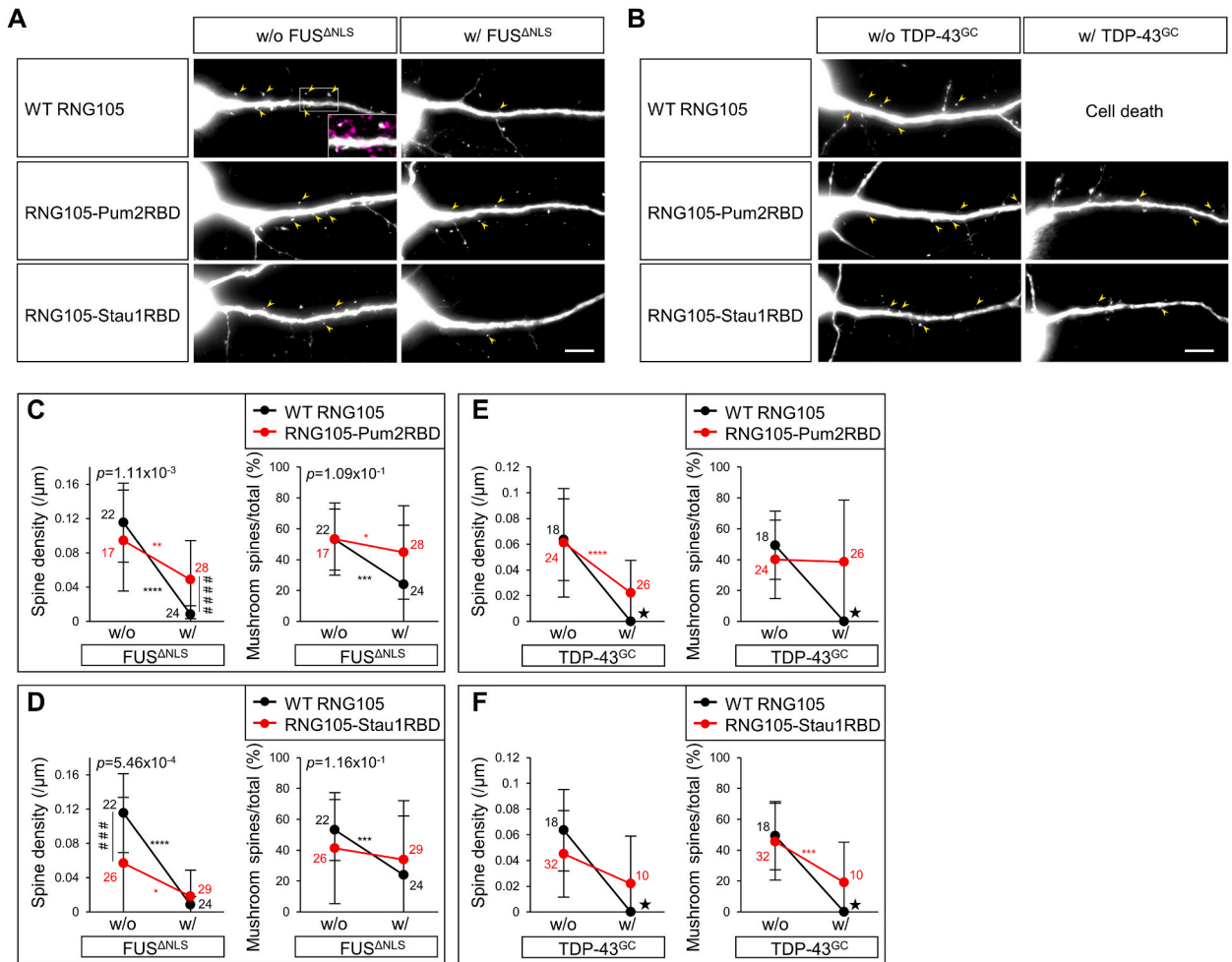

Fig. 9. Substitution of RNG105 RBD1 suppresses the impairment of spine formation caused by the combination of FUS$^{\Delta NLS}$/TDP-43^{G348C} and WT RNG105. (A and B) Representative images of dendritic spines of cultured neurons expressing untagged WT and RBD1-substituted mutants of RNG105, with and without expression of untagged FUS$^{\Delta NLS}$ or TDP43^{GC}. The spines are visualized by GFP expression. The inset shows a magnified image of the boxed area, showing that the spines are attached to the synaptic marker synapsin I (magenta). Arrowheads indicate the synapsin I-attached spines. Scale bars, 10 μm. **(C–F)** Spine density and the ratio of the number of mushroom spines to the total spines. The data are stated as the mean ± S.D. The number of neurons analyzed from 4 independent cultures is shown in the graph. The p-values for the interaction effect in two-way ANOVA are indicated. *p < 0.05, **p < 0.01, ***p < 0.005, ****p < 0.001, ###p < 0.005, ####p < 0.001, post-hoc Student's t-test after two-way ANOVA. Because most of the neurons in the groups indicated by the stars were dead, statistical analysis of those groups was not possible. See also Figs. S16 and S17.

In human patients, point mutations in FUS and TDP-43 have been identified. FUS pathogenic mutations frequently occur in the C-terminal nuclear localization signal (NLS), such as FUS^{R514G}, FUS^{R522G}, FUS^{P525L}, and FUS^{R495X}. These mutants translocate to the cytoplasm and promote the formation of cytoplasmic RNA-containing granules [61,62]. Notably, although FUS^{P525L} increases cytoplasmic translocation, it does not itself increase aggregation propensity [62], which may be a common feature of FUS NLS mutants including FUS$^{\Delta NLS}$ lacking the C-terminal 17 amino acids used in this study. In contrast, FUS^{G156E}, whose mutation is located in the

QGSY-rich domain (a.k.a. PrLD), tends to transition to less dynamic fibers [34]. However, this mutant localizes to the nucleus and its aggregation occurs predominantly in the nucleus, suggesting that the toxicity of this mutant is exerted through nuclear aggregation rather than cytoplasmic mislocalization [62,63].

Disease-related TDP-43 mutations are often found in the C-terminal G-rich domain, also known as PrLD. Although these mutations do not significantly enhance cytoplasmic translocation or cytoplasmic granule formation, certain mutants such as TDP-43^{M337V} and TDP-43^{G348C} tend to be retained in sorbitol-induced stress granules, suggesting their slower dissolution from those granules [40,64]. Even in the absence of stress, TDP-43^{G348C} forms cytoplasmic granules in primary spinal cord neurons in a cell-type-specific manner [41].

Challenges have been made to reproduce the effects of the human disease-associated mutants in mice. Knock-in mice with physiological expression levels sometimes showed no disease phenotype, even mice with the less dynamic TDP-43^{M337V} mutation [65]. However, transgenic mice with these mutations have demonstrated dose-dependent deterioration of the phenotypes [18,19,65,66]. Interestingly, disease phenotypes have been reproduced in WT FUS and TDP-43 transgenic mice [16,17], and phenotype-causing expression levels are often comparable between WT and mutants including TDP-43^{M337V} [18,19]. These studies suggest that excess FUS and TDP-43 can mimic human pathology in mice, regardless of mutations. Such increased expression and cytoplasmic granule formation of WT FUS and TDP-43 have also been reported in human patients [11,20].

Also in this study, the effects of WT FUS and TDP-43 were essentially the same as those of the mutants, FUS$^{\Delta NLS}$ and TDP-43^{G348C}, in any assay. These similarities between WT and mutants suggest that the effects do not arise from mutant-specific alterations in biochemical activities, molecular interactions, or dominant negative effects, but rather from similar pathogenic mechanisms between them, such as exceeding a saturation concentration level for phase separation and subsequent granule formation in the cytoplasm [3, 13]. The concentration of FUS and TDP-43 in dense liquid granules, even if they are WT proteins, would increase the probability of liquid-to-solid phase transition. However, we noted that FUS and FUS$^{\Delta NLS}$ in the granules exhibited relatively high fluidity in the cell permeabilization assays (Fig. 3A), suggesting that the effects observed in this study occurred before granule maturation into irreversible aggregates.

RBD1 of RNG105 is a coiled-coil RBD, has no homology to other RBDs, and is exclusive to RNG proteins, including vertebrate RNG105 and RNG140, as well as invertebrate RNGI [50]. This may explain why the high sensitivity to FUS and TDP-43 was unique to RNG105 among the tested RBPs, although it does not exclude the possibility of other types of domains with similar characteristics. It may be a little surprising that the folded domain, not the IDR, regulates the assembly and dissociation with the condensates, but similar cases have been reported in which folded domains regulate phase separation and are utilized for opto-manipulation of phase separation [67,68].

We propose that the sensitivity of RNG105 to FUS and TDP-43 may be attributed to the equilibrium of co-phase separation of its RBP1 with RNA granule components being biased towards dissociation. This appears to be contrary to the effect of RNG105 on FUS in fibroblasts, where RNG105 increases FUS dynamics [45]. However, the equilibrium of phase separation depends on several factors, including the composition and concentration of the components in condensates and their post-translational modifications. Therefore, the differences in the effects of RNG105 and FUS on each other between neurons and fibroblasts may be due to the different conditions for assembling RNA granules in these cell types, which may be inferred from the marked difference that endogenous RNA granules are not formed in fibroblasts but in neurons at a steady state without stress. The differences between the cell types may also explain the ability of RNG105-ΔRBP1 to assemble RNA granules in neurons but not in fibroblasts [56].

The co-aggregation of FUS and TDP-43 with RNA granule components has been implicated in their toxic effects on neural function by suppressing or sequestrating essential components. However, the components reported to have constrained movement within the granules have been limited to proteins such as survival motor neuron (SMN) and Stau1 [36], and it has remained elusive whether many other components are similarly regulated. In contrast to the co-aggregation model, our findings suggest that FUS and TDP-43 increase the dynamics of RNG105, dissociating it from RNA granules. In general, biomolecular condensates can regulate biochemical reactions in various ways [69,70], such as accelerating reactions through condensation of factors required for the reaction, or suppressing reactions by excluding some components from the condensate. Inactivation of biochemical reactions can also occur by shifting the phase of the condensate from liquid to gel or solid. The last example corresponds to the co-aggregation model, whereas the exclusion of the required factors, such as RNG105 and its associated molecules, from RNA granules provides a novel model of FUS- and TDP-43-induced RNA granule dysfunction.

The dynamic properties of RNG105 RBD1 appear to pose a risk as they mediate the defects caused by pathogenic cytoplasmic FUS and TDP-43. However, this risk may be a trade-off with biological advantages in healthy conditions because, in the absence of FUS or TDP-43 overexpression, the less dynamic mutant RNG105-Stau1RBD reduced local translation in RNA granules and attenuated dendritic spine formation. Nevertheless, the non-dissociable RNG105 mutants exhibited suppressive effects on the neurotoxicity of overexpressed FUS and TDP-43, providing the basis for understanding and treating cognitive impairment in neurodegenerative diseases.

4. Limitations of the study

Substitution of the RBD1 of RNG105 with the RBDs of Pum2 and Stau1 restored its localization to RNA granules and recruitment of mRNA in the presence of FUS and TDP-43, but it remains elusive whether the RBD1 substitution altered mRNA specificity in the granules. Since RNG105 uses not only RBD1 but also IDRs such as RBD2 and E-rich domain to recruit mRNAs through co-phase separation with mRNAs, mRNA specificity may not be determined solely by RBD1. Addressing this issue will require spatial transcriptomics using such as APEX-seq and photo isolation chemistry (PIC) [71,72]. Nevertheless, this study suggested that the

RBD1-substituted mutants recruit at least SunTag mRNA harboring the *Arc* 3'UTR to granules, similar to WT RNG105.

This study used an overexpression system in primary cultured neurons, and it is not certain whether the effects observed here occur similarly at the individual level in neurodegenerative diseases. It has been reported that FUS[ΔNLS] and TDP-43[G348C] transgenic mice, as well as WT FUS and TDP-43 transgenic mice and rats, exhibit memory deficits reminiscent of ALS and FTD ([43,44,73–75]). The use of these mice, as well as mutant FUS and TDP-43 knock-in mice that express them less than in transgenic mice, will allow us to validate the RNG105-mediated local translation mechanism and its effects on pathology *in vivo*.

Author contribution statement

Tomoyo Horio: Conceived and designed the experiments; Performed the experiments; Analyzed and interpreted the data; Wrote the paper.

Yui Ishikura: Performed the experiments.

Rie Ohashi: Contributed reagents, materials, analysis tools or data.

Nobuyuki Shiina, Ph.D.: Conceived and designed the experiments; Wrote the paper.

5. Data availability statement

Data will be made available on request.

STAR methods

Resource availability

Lead contact

Further information and requests for resources and reagents should be directed to and will be fulfilled by the lead contact, Nobuyuki Shiina (nshiina@nibb.ac.jp).

Material availability

Plasmids generated in this study are available from the lead contact with a completed Material Transfer Agreement.

Data and code availability

All data reported in this paper will be shared by the lead contact upon request.

This paper does not report original code.

Any additional information required to reanalyze the data reported in this paper is available from the lead contact upon request.

Experimental model and subject details

Mice

ICR mouse embryos at embryonic day 16 (E16) were used for neuron cultures. All animal care and experiments were approved by the Animal Experiment Committee of National Institutes of Natural Sciences (22A005), and performed following the guidelines from the National Institutes of Natural Sciences and the Science Council of Japan.

Method details

Neuron culture and transfection

Dissociated cerebral cortical neurons were prepared from E16 mouse embryos. Neurons were plated onto poly-D-lysine-coated coverslips in glass-bottomed dishes (MatTek, Ashland, MA) using Neurobasal-A medium (Thermo Fisher Scientific, Waltham, MA) containing B-27 supplement (Thermo Fisher Scientific), 0.5 mM glutamine, and 25% Neuron Culture Medium (FUJIFILM Wako Pure Chemical, Osaka, Japan) at a density of 1.6×10^6 cells/cm^2. Cultures were incubated at 37 °C in a 5% CO$_2$ incubator. Neurons were transfected with plasmids at 6 DIV, or 7 DIV for morphological analysis of dendritic spines, using conventional calcium-phosphate transfection methods. Transfected neurons were observed 1 day after transfection or 3–4 days after transfection in knockdown experiments and morphological analysis of dendritic spines.

Plasmid construction

The pCAG-GFP vector (Addgene, Watertown, MA) was used to construct all the plasmids for expressing RBPs in neurons. DNA fragments, obtained by PCR from each template using each primer set, were cloned into the EcoRI and NotI sites of the pCAG-GFP

vector using the In-Fusion Cloning Kit (Takara Bio, Shiga, Japan). Notably, cloning into the EcoRI and NotI sites of the vector removed the GFP-coding sequence that the vector originally had. The PCR templates and primer sets are listed in the supplementary tables (Tables S1–S3). After cloning into the vector, we checked all the sequences of the inserts. When RBPs were tagged with GFP, mRFP1, and Sirius, these fluorescent proteins were tagged at the C-termini of the RBPs through three- or five-glycine linkers. G348C mutation in TDP-43 was introduced using the QuikChange Lightning Multi Site-Directed Mutagenesis Kit (Agilent Technologies, Santa Clara, CA).

DNA fragments encoding scFv (fluorescent single-chain variable fragment)-sfGFP-GB1 and 24xV4 (24 tandem array of V4 peptides)-ODC (ornithine decarboxylase)-*Arc* 3'UTR [51] were cloned into the EcoRI and NotI sites of the pCAG-GFP vector (Addgene) for use in the SunTag analysis as follows. The DNA fragment encoding scFv-sfGFP-GB1 was obtained by PCR from the pFUGW-scFv-sfGFP-GB1 plasmid [51] using primers 5'- ttttggcaaagaattgtcgccaccatgggccccga-3' and 5'-ctgaggagtgcggccttattcggt-taccgtgaagg-3'. The fragment was cloned into the EcoRI and NotI sites of the pCAG-GFP vector using the In-Fusion Cloning Kit. To construct the 24xV4-ODC-*Arc* 3'UTR plasmid, first, a DNA fragment encoding the *Arc* 3'UTR was obtained by PCR from the pFUGW-24xV4-ODC-*Arc* 3'UTR plasmid [51] using primers 5'-ttttggcaaagaattctaccggtttttttgctagcaggggccagcccagggtccc-3' and 5'-ctgaggagtgcggccaacaaaatcatatatagata-3', which introduced AgeI and NheI sites 5'-upstream of *Arc* 3'UTR. The fragment was cloned into the EcoRI and NotI sites of the pCAG-GFP vector using the In-Fusion Cloning Kit. Next, a DNA fragment encoding 24xV4-ODC was cloned into the newly introduced AgeI and NheI sites of the plasmid by T4 DNA ligation. For this purpose, the NheI site was introduced into the pFUGW-24xV4-ODC plasmid as follows. Two DNA fragments with their ends overlapping were obtained by PCR from the pFUGW-24xV4-ODC plasmid using the primer sets 5'-ctaagaattatcatctcgagaacgagg-3' and 5'-cggctagctagtgtgtacattaca-cattgatcctagcag-3', and 5'-aatgtacacactagctagccgatatcaagcttatcgataatc-3' and 5'-gttttttctaggtctcgaggtc-3', which introduced the NheI site into the overlapping region of the two fragments. The original sequence of the pFUGW-24xV4-ODC plasmid was replaced with the two fragments by digesting the plasmid with XhoI and inserting the fragments using the In-Fusion Cloning Kit. From the resulting plasmid, the 24xV4-ODC-coding region was excised using the original AgeI site and the newly introduced NheI site. This DNA fragment was cloned into the AgeI and NheI sites of the pCAG-*Arc* 3'UTR plasmid by T4 DNA ligation to obtain the 24xV4-ODC-*Arc* 3'UTR plasmid. After cloning into the vector, we checked all the sequences of the inserts.

The pH1'-DsRed2-I-P vector [76] was used to construct the shRNA plasmids for RBPs knockdown in neurons. Two plasmids were constructed for each RBP. DNA inserts were cloned into the PstI and XbaI sites of the vector. The plasmids were designed to contain the inserts below, with the target sense and antisense sequences underlined. The target sequences had no homology to other transcripts when analyzed using BLAST (http://blast.ncbi.nlm.nih.gov/Blast.cgi). 5'- ccc<u>gcctgtgtgtggaacaacctattc</u>aagagat<u>aggttgttccacaca-caggc</u>tttttggaaa-3' and 5'- ccc<u>ggcagcgtgtacaagatcttattc</u>aagagat<u>aagatcttgtacacgctgcc</u>tttttggaaa-3' for RNG105, 5'- ccc<u>gcaa-caaagctacggacaattc</u>aagagat<u>tgtccgtagctttgttgct</u>tttttggaaa-3' and 5'- ccc<u>gagtggaggttatggtcaattc</u>aagagat<u>tgaccataacctccactc</u>tttttggaaa-3' for FUS, and 5'- ccc<u>ggttcttatggttcaggtcaattc</u>aagagat<u>tgacctgaaccataagaacc</u>tttttggaaa-3' and 5'- ccct<u>ggatgagacagatgcttc</u>ttcaagaga-<u>gaagcatctgtctcatcca</u>tttttggaaa-3' for TDP-43.

Fluorescence imaging of RBPs in dendrites and quantitative analysis of RBP accumulation in RNA granules

Neurons expressing GFP- and mRFP1-tagged RBPs were fixed with 3.7% formaldehyde in phosphate-buffered saline (PBS) for 10 min. After washing with PBS, the specimens were mounted in Mowiol (Sigma-Aldrich, Burlington, MA). Fluorescence images were acquired using an A1 confocal laser scanning microscope equipped with a Ti-E inverted microscope (Nikon, Tokyo, Japan) and a PlanApo VC 60 × water immersion objective. The fluorescence intensity of the images was measured using ImageJ. To measure the accumulation of RBPs in the granules in dendrites, the images were smoothed with a mean filter using ImageJ. Then, fluorescence intensity within a single granule was measured along a line parallel to the dendrite across the fluorescence peak of the granule to draw a fluorescence intensity curve. The difference in fluorescence intensity between two adjacent pixels at half the maximum fluorescence intensity of the curve was calculated as the slope (Fig. 1B, right schematic). The granule/cytoplasm partition coefficient of RNG105 was calculated as $(F_g\text{-}F_b)/(F_c\text{-}F_b)$, where F_g, F_c, and F_b are the fluorescence intensities of RNG105 in granules, cytoplasm, and extra-cellular areas (background), respectively.

FRAP analysis

Time-lapse fluorescence images of mRFP1- or GFP-tagged RBPs in neurons were acquired at 5-sec intervals using the A1 confocal laser scanning microscope with the PlanApo VC 60 × water immersion objective. Four control images were taken before bleaching. Then, an elliptical ROI covering the whole area of one RNA granule in the dendrite was bleached using the 561-nm laser (10 mW) or 488-nm laser (40 mW) at 60% power and 8 s/frame. ImageJ was used to measure the fluorescence intensity at each time point for the RNA granule within the ROI (F), the other granules in the same neuron (F_g), and the cytoplasm of the dendrite (F_c). The fluorescence intensity of the target RNA granule at each time point ($F_{(t)}$) was normalized as shown in Equation (1), where $t = 0$ is just after photobleaching.

$$F_{(t)} = \left((F - F_c)_{(t)} - (F - F_c)_{(t=0)} \right) \Big/ (F_g - F_c)_{(t)} \tag{1}$$

Then, the fluorescence intensity (% relative to before bleaching) was calculated as $F_{(t)}/F_{cont}$, where F_{cont} is the average of the $F_{(t)}$ of the four control images obtained before bleaching. These values ($F_{(t)}/F_{cont}$, $t \geq 0$) were fitted with Equation 2, where F_m is the mobile fraction (maximum recovery) and $\tau_{1/2}$ is the halftime of recovery. The least-squares method with Excel Solver was used for fitting.

$$f_{(t)} = F_m \left(1 - e^{-\frac{\ln 2}{\tau_{1/2}} t} \right) \tag{2}$$

Cell permeabilization analysis

Time-lapse fluorescence images were acquired at 5-sec intervals for GFP- and mRFP1-tagged RBPs in neurons using an IX83 inverted microscope (Olympus, Tokyo, Japan) with a PlanApo 60 × oil objective and the Prime 4.2 Megapixel sCMOS camera (Teledyne Photometrics, Tucson, AZ). After taking 10 images, 0.5 ml of 0.075% digitonin dissolved in the medium was added to the neurons cultured in 2 ml of the same medium. After adding digitonin, fluorescence images were taken at 5-sec intervals for about 300 s. The fluorescence intensity of the RNA granules in the dendrite (F_g) was measured using ImageJ. The decrease in fluorescence intensity of the dendritic RNA granule at each time point ($F_{(t)}$) was calculated as shown in Equation 3, where $t = 0$ is just before the neuron became permeable.

$$F_{(t)} = F_{g(t)} - F_{g(t=0)} \tag{3}$$

Then, the decrease in fluorescence intensity (% relative to before permeabilization) was calculated as $F_{(t)}/F_{cont}$, where F_{cont} is the average of the granule fluorescence before permeabilization ($F_{(t)}$, $t \leq 0$). The fluorescence intensity curve of the measured value ($-F_{(t)}/F_{cont}$, $t \geq 0$) was fitted with Equation 2, where F_m is the mobile fraction (maximum dissolution from RNA granules) and $\tau_{1/2}$ is the halftime of dissolution from RNA granules. The least-squares method with Excel Solver was used for fitting.

Immunocytochemistry

Neurons were fixed at 7 DIV with 3.7% formaldehyde in PBS for 10 min. After washing with PBS, the neurons were treated with 0.5% Triton X-100 in PBS for 10 min. After washing with PBS and blocking with 10% FBS in Dulbecco's modified Eagle's medium (DMEM), the specimens were incubated with primary antibodies: rabbit anti-RNG105 [56], biotinylated rabbit anti-RNG105 [56], rabbit anti-FMRP (ab17722, Abcam, Cambridge, UK), mouse anti-FMRP (MAB2160, Merck Millipore, Burlington, MA), rabbit anti-Staufen [77], rabbit anti-Dcp2 [78], rabbit anti-Xrn1 [79], mouse anti-FUS (60160-1-Ig, Proteintech Group, Rosemont, IL), mouse anti-TDP-43 (60019-2-Ig, Proteintech Group), mouse anti-TDP-43 (ab104223, Abcam), and mouse anti-Ribosomal protein S6 (#2317, Cell Signaling Technology, Danvers, MA) antibodies. Neurons were then washed with PBS and stained with secondary antibodies: Alexa 488-conjugated anti-rabbit IgG (Thermo Fisher Scientific), Cy3-conjugated anti-rabbit IgG (Jackson ImmunoResearch, West Grove, PA), Cy5-conjugated anti-rabbit IgG (Jackson ImmunoResearch), DyLight405-conjugated anti-mouse IgG (Jackson ImmunoResearch), Alexa 488-conjugated anti-mouse IgG (Thermo Fisher Scientific), Cy3-conjugated anti-mouse IgG (Jackson ImmunoResearch), and DyLight649-conjugated anti-mouse IgG (Jackson ImmunoResearch) antibodies. Staining with the biotinylated anti-RNG105 antibody and Alexa 488-conjugated streptavidin (Thermo Fisher Scientific) was performed after the specimens were stained with other antibodies and refixed with formaldehyde. After washing with PBS, the specimens were mounted in Mowiol. Fluorescence images were acquired using the A1 confocal laser scanning microscope with the PlanApo VC 60 × water immersion objective.

In situ hybridization

Neurons were fixed with 3.7% formaldehyde in PBS containing 5 mM MgCl$_2$ (PBSM) for 10 min. After washing with PBSM, neurons were treated with 0.5% Triton X-100 in PBSM for 10 min. Then, the neurons were washed with PBSM, equilibrated with 15% formamide, 2 × saline-sodium citrate (SSC), and 10 mM sodium phosphate (pH 7.0) for 10 min. They were probed with 0.25 µg/ml 3'-digoxigenin-labeled poly (dT) probe (55-mer), SunTag antisense probes (mixture of 5'-tttttaatcgagcgacctcattttcaagatgatagttcttcga-gagcagttcctc-3' and 5'-ttttcaacctggcgacctcattttcgaggtggtagttcttcgataagagttcttc-3'), or SunTag sense probes (mixture of 5'-gag-gaactgctctcgaagaactatcatcttgaaaatgaggtcgctcgattaaaaa-3' and 5'-gaagaactcttatcgaagaactaccacctcgaaaatgaggtcgccaggttgaaaa-3') in 0.5 mg/ml yeast t-RNA (Roche, Basel, Switzerland), 0.5 mg/ml salmon sperm DNA (Sigma-Aldrich), 10% dextran sulfate, 0.1% BSA, 15% formamide, 2 × SSC, and 10 mM sodium phosphate (pH 7.0) at 37 °C for 1.5 h. The neurons were washed with 15% formamide and 2 × SSC at 37 °C for 20 min, and then, with 1 × SSC for 30 min. After blocking with 10% FBS in DMEM, the probes were labeled with an anti-digoxigenin antibody (Roche) and an Alexa 647-conjugated anti-sheep IgG antibody (Jackson ImmunoResearch). After washing with PBS, the specimens were mounted in Mowiol. Fluorescence images were acquired using the A1 confocal laser microscope with the PlanApo VC 60 × water immersion objective. The fluorescence intensity of the labeled mRNA in the dendritic granules where RNG105 was localized was measured and normalized by the fluorescence intensity of the dendrites of neighboring untransfected neurons.

Translation analysis in RNA granules using the SunTag system

Neurons were transfected with scFv-sfGFP-GB1 and 24xV4-ODC-Arc 3'UTR. They were fixed with 3.7% formaldehyde in PBS for 10 min, washed with PBS, and then, the specimens were mounted in Mowiol. Fluorescence images were acquired using a TCS SP8 MP confocal microscope equipped with a DMI6000CS inverted microscope (Leica Microsystems, Wetzlar, Germany) and an HC PL APO 63 × /1.20 W CORR CS2 water immersion objective. The GFP fluorescence in the dendritic granules was measured and normalized by min-max normalization in each neuron. In these analyses, we noted that fluorescence images of co-expressed Sirius-tagged RBPs were noisy due to the laser wavelength (405 nm) used for Sirius (excitation peak: 355 nm).

Morphological analysis of dendritic spines

RBPs-transfected neurons were co-transfected with the pEGFP-N1 plasmid to visualize dendritic spines with GFP. They were fixed at 11 DIV for FUS$^{\Delta NLS}$-transfected neurons, or 10 DIV for TDP-43^{G348C}-transfected neurons, with 3.7% formaldehyde in PBS for 10 min. After washing with PBS, the neurons were treated with 0.5% Triton X-100 in PBS for 10 min. After washing with PBS and blocking with 10% FBS in DMEM, presynapses were labeled with an anti-synapsin I antibody (Merck Millipore) and a Cy3-conjugated anti-rabbit IgG

antibody (Jackson ImmunoResearch). After washing with PBS, the specimens were mounted in Mowiol. Fluorescence images were acquired using the IX83 inverted microscope with the PlanApo 60 × oil objective and the Prime 4.2 Megapixel sCMOS camera. The images were analyzed using ImageJ. Dendritic protrusions where synapsin I was attached were deemed to be spines. The number of spines was counted along the dendrites and normalized by the length of the dendrites. The mushroom spine was defined as having a maximum head width/neck width ratio of 1.5 or greater, which is often used as a cutoff value [80,81].

Quantification and statistical analysis

The data are represented as scatter plots showing all the individual values, which are stated as the mean ± S.D. The number of samples is shown in the figures. Statistical analysis was performed using R. Significance was determined using one-way ANOVA followed by the Tukey-Kramer test and two-way ANOVA followed by post-hoc Student's t-test, as indicated in the figure legends.

Key Resources Table

REAGENT or RESOURCE	SOURCE	IDENTIFIER
Antibodies		
Rabbit polyclonal anti-RNG105	Shiina et al., 2005	N/A
Biotinylated rabbit polyclonal anti-RNG105	Shiina et al., 2005	N/A
Rabbit polyclonal anti-FMRP	Abcam	Cat#ab17722; RRID: AB_2278530
Mouse monoclonal anti-FMRP	Millipore	Cat#MAB2160; RRID: AB_2283007
Rabbit polyclonal anti-Staufen	Marión et al., 1999	N/A
Rabbit polyclonal anti-Dcp2	Wang et al., 2002	N/A
Rabbit polyclonal anti-Xrn1	Bashkirov et al., 1997	N/A
Mouse monoclonal anti-FUS	Proteintech	Cat#60160-1-Ig; RRID: AB_10666169
Mouse monoclonal anti-TDP-43	Proteintech	Cat#60019-2-Ig; RRID: AB_2200520
Mouse monoclonal anti-TDP-43	Abcam	Cat#ab104223; RRID: AB_10710019
Mouse monoclonal anti-Ribosomal protein S6	Cell Signaling Technology	Cat#2317; RRID: AB_2238583
Sheep polyclonal anti-digoxigenin	Roche	Cat#11333089001; RRID: AB_514496
Rabbit polyclonal anti-synapsin I	Millipore	Cat#AB1543; RRID: AB_2200400
Alexa 488-conjugated anti-rabbit IgG	Thermo Fisher Scientific	Cat#A-11034; RRID: AB_2576217
Cy3-conjugated anti-rabbit IgG	Jackson ImmunoResearch	Cat#711-165-152; RRID: AB_2307443
Cy5-conjugated anti-rabbit IgG	Jackson ImmunoResearch	Cat#111-175-144; RRID: AB_2338013
DyLight405-conjugated anti-mouse IgG	Jackson ImmunoResearch	Cat#715-475-150; RRID: AB_2340839
Alexa 488-conjugated anti-mouse IgG	Thermo Fisher Scientific	Cat#A-11029; RRID: AB_2534088
Cy3-conjugated anti-mouse IgG	Jackson ImmunoResearch	Cat#715-165-150; RRID: AB_2340813
DyLight 649-conjugated anti-mouse IgG	Jackson ImmunoResearch	Cat#715-495-151
Alexa 647-conjugated anti-sheep IgG	Jackson ImmunoResearch	Cat#713-605-147; RRID: AB_2340751
Chemicals, peptides, and recombinant proteins		
Neurobasal-A medium	Thermo Fisher Scientific	Cat#10888022
B-27 supplement	Thermo Fisher Scientific	Cat#17504044
Neuron Culture Medium	FUJIFILM Wako Pure Chemical	Code: 148-09671
Mowiol 4-88	Sigma-Aldrich	Cat#81381
Yeast t-RNA	Roche	Cat#10109495001
Salmon sperm DNA	Sigma-Aldrich	Cat#D1626
L-Glutamine	Thermo Fisher Scientific	Cat#21051024
Formaldehyde	FUJIFILM Wako Pure Chemical	Code: 064-00406
Digitonin	FUJIFILM Wako Pure Chemical	Code: 048-02124

(*continued*)

REAGENT or RESOURCE	SOURCE	IDENTIFIER
Triton X-100	Sigma-Aldrich	Cat#T8787
Dulbecco's Modified Eagle's Medium	Sigma-Aldrich	Cat#D5796
Alexa 488-conjugated streptavidin	Thermo Fisher Scientific	Cat#S11223
Dextran sulfate	FUJIFILM Wako Pure Chemical	Code: 197-08362
BSA	FUJIFILM Wako Pure Chemical	Code: 015-20951
Critical commercial assays		
In-Fusion HD Cloning Kit	Takara Bio	Code: 639650
QuikChange Lightning Multi Site-Directed Mutagenesis Kit	Agilent Technologies	Cat#210513
Experimental models: Organisms/strains		
Mouse: Jcl:ICR	CLEA Japan	N/A
Oligonucleotides		
Primers for RBPs, see Tables S1–S3	This paper	N/A
Primer: scFv-sfGFP-GB1 Forward: TTTTGGCAAAGAATTGTCGCCACCATGGGCCCCGA	This paper	N/A
Primer: scFv-sfGFP-GB1 Reverse: CTGAGGAGTGCGGCCTTATTCGGTTACCGTGAAGG	This paper	N/A
Primer: Arc 3'UTR Forward: TTTTGGCAAAGAATTCTACCGGTTTTTTTGCTAGCAGGGGCCAGCCCAGGGTCCC	This paper	N/A
Primer: Arc 3'UTR Reverse: CTGAGGAGTGCGGCCAACAAAATCATATATAGATA	This paper	N/A
Primer: 24xV4-ODC Forward 1: CTAAGAATTATCATCTCGAGAACGAGG	This paper	N/A
Primer: 24xV4-ODC Reverse 1: CGGCTAGCTAGTGTGTACATTACACATTGATCCTAGCAG	This paper	N/A
Primer: 24xV4-ODC Forward 2: AATGTACACACTAGCTAGCCGATATCAAGCTTATCGATAATC	This paper	N/A
Primer: 24xV4-ODC Reverse 2: GTTTTTCTAGGTCTCGAGGTC	This paper	N/A
Insert: RNG105 shRNA-1: CCCGCCTGTGTGTGGAACAACCTATTCAAGAGATAGGTTGTTCCACACACAGGCTTTTTGGAAA	This paper	N/A
Insert: RNG105 shRNA-2: CCCGGCAGCGTGTACAAGATCTTATTCAAGAGATAAGATCTTGTACACGCTGCCTTTTTGGAAA	This paper	N/A
Insert: FUS shRNA-1: CCCGCAACAAAGCTACGGACAATTCAAGAGATTGTCCGTAGCTTTGTTGCTTTTTGGAAA	This paper	N/A
Insert: FUS shRNA-2: CCCGAGTGGAGGTTATGGTCAATTCAAGAGATTGACCATAACCTCCACTCTTTTTGGAAA	This paper	N/A
Insert: TDP-43 shRNA-1: CCCGGTTCTTATGGTTCAGGTCAATTCAAGAGATTGACCTGAACCATAAGAACCTTTTTGGAAA	This paper	N/A
Insert: TDP-43 shRNA-2: CCCTGGATGAGACAGATGCTTCTTCAAGAGAGAAGCATCTGTCTCATCCATTTTTGGAAA	This paper	N/A
3'-digoxigenin-labeled poly (dT) probe (55-mer)	This paper	N/A
3'-digoxigenin-labeled SunTag antisense probe-1: TTTTTAATCGAGCGACCTCATTTTCAAGATGATAGTTCTTCGAGAGCAGTTCCTC	This paper	N/A
3'-digoxigenin-labeled SunTag antisense probe-2: TTTTCAACCTGGCGACCTCATTTTCGAGGTGGTAGTTCTTCGATAAGAGTTCTTC	This paper	N/A
3'-digoxigenin-labeled SunTag sense probe-1: GAGGAACTGCTCTCGAAGAACTATCATCTTGAAAATGAGGTCGCTCGATTAAAAA	This paper	N/A
3'-digoxigenin-labeled SunTag sense probe-2: GAAGAACTCTTATCGAAGAACTACCACCTCGAAAATGAGGTCGCCAGGTTGAAAA	This paper	N/A
Recombinant DNA		
pCAG-GFP	Addgene	Cat#11150; RRID: Addgene_11150
PCR template Plasmids for RBPs, see Tables S1–S3	This study	N/A
Plasmids of pCAG-RBPs, see Tables S1–S3	This study	N/A
pFUGW-scFv-sfGFP-GB1	Wang et al., 2016	N/A
pFUGW-24xV4-ODC-Arc 3'UTR	Wang et al., 2016	N/A
pCAG-scFv-sfGFP-GB1	This study	N/A
pCAG-24xV4-ODC-Arc 3'UTR	This study	N/A
pH1'-DsRed2-I-P	Takahashi et al., 2007	N/A
pEGFP-N1	Clontech	https://www.addgene.org/vector-database/2491/
Software and algorithms		
NCBI BLAST		http://blast.ncbi.nlm.nih.gov/Blast.cgi
ImageJ		https://imagej.net/
Excel Solver		http://www.solver.com/
R		https://www.r-project.org

Declaration of competing interest

The authors declare that they have no known competing financial interests or personal relationships that could have appeared to influence the work reported in this paper.

Acknowledgments

We would like to thank Dr. D. Ito for the generous gift of human FUS plasmid; Dr. X. Zhuang for the generous gift of pFUGW-scFv-sfGFP-GB1 and pFUGW-24xV4-ODC-*Arc* 3'UTR plasmids; Dr. K. Kato for his advice on the quantitative analysis of RBP accumulation in RNA granules; the Optics and Imaging Facility in the NIBB Trans-Scale Biology Center for technical supports. This work was supported by the Grant-in-Aid for Scientific Research (19H03161 and 22H02552) from the Japan Society for the Promotion of Science (JSPS) and the Bioscience Research Grant from the Takeda Science Foundation to N.S.

Appendix A. Supplementary data

Supplementary data to this article can be found online at https://doi.org/10.1016/j.heliyon.2023.e17065.

References

[1] R. Ferrari, D. Kapogiannis, D. Edward, E.D. Huey, P. Momeni, FTD and ALS: a tale of two diseases, Curr. Alzheimer Res. 8 (2011) 273–294, https://doi.org/10.2174/156720511795563700.

[2] M.A. van Es, O. Hardiman, A. Chio, A. Al-Chalabi, R.J. Pasterkamp, J.H. Veldink, L.H. van den Berg, Amyotrophic lateral sclerosis, Lancet 390 (2017) 2084–2098, https://doi.org/10.1016/S0140-6736(17)31287-4.

[3] S.C. Ling, M. Polymenidou, D.W. Cleveland, Converging mechanisms in ALS and FTD: disrupted RNA and protein homeostasis, Neuron 79 (2013) 416–438, https://doi.org/10.1016/j.neuron.2013.07.033.

[4] A. Brun, X. Liu, C. Erikson, Synapse loss and gliosis in the molecular layer of the cerebral cortex in Alzheimer's disease and in frontal lobe degeneration, Neurodegeneration 4 (1995) 171–177, https://doi.org/10.1006/neur.1995.0021.

[5] G. Shiihashi, D. Ito, I. Arai, Y. Kobayashi, K. Hayashi, S. Otsuka, K. Nakajima, M. Yuzaki, S. Itohara, N. Suzuki, Dendritic homeostasis disruption in a novel frontotemporal dementia mouse model expressing cytoplasmic fused in sarcoma, EBioMedicine 24 (2017) 102–115, https://doi.org/10.1016/j.ebiom.2017.09.005.

[6] C.M. Henstridge, D.I. Sideris, E. Carroll, S. Rotariu, S. Salomonsson, M. Tzioras, C.A. McKenzie, C. Smith, C.A.F. von Arnim, A.C. Ludolph, D. Lulé, D. Leighton, J. Warner, E. Cleary, J. Newton, R. Swingler, S. Chandran, T.H. Gillingwater, S. Abrahams, T.L. Spires-Jones, Synapse loss in the prefrontal cortex is associated with cognitive decline in amyotrophic lateral sclerosis, Acta Neuropathol. 135 (2018) 213–226, https://doi.org/10.1007/s00401-017-1797-4.

[7] C.F. Sephton, A.A. Tang, A. Kulkarni, J. West, M. Brooks, J.J. Stubblefield, Y. Liu, M.Q. Zhang, C.B. Green, K.M. Huber, E.J. Huang, J. Herz, G. Yu, Activity-dependent FUS dysregulation disrupts synaptic homeostasis, Proc. Natl. Acad. Sci. USA 111 (2014) E4769–E4778, https://doi.org/10.1073/pnas.1406162111.

[8] M.J. Fogarty, E.W. Mu, P.G. Noakes, N.A. Lavidis, M.C. Bellingham, Marked changes in dendritic structure and spine density precede significant neuronal death in vulnerable cortical pyramidal neuron populations in the SOD1G93A mouse model of amyotrophic lateral sclerosis, Acta Neuropathol. Commun. 4 (2016) 77, https://doi.org/10.1186/s40478-016-0347-y.

[9] G.H. Gorrie, F. Fecto, D. Radzicki, C. Weiss, Y. Shi, H. Dong, H. Zhai, R. Fu, E. Liu, S. Li, H. Arrat, E.H. Bigio, J.F. Disterhoft, M. Martina, E. Mugnaini, T. Siddique, H.X. Deng, Dendritic spinopathy in transgenic mice expressing ALS/dementia-linked mutant UBQLN2, Proc. Natl. Acad. Sci. USA 111 (2014) 14524–14529, https://doi.org/10.1073/pnas.1405741111.

[10] A. Starr, R. Sattler, Synaptic dysfunction and altered excitability in C9ORF72 ALS/FTD, Brain Res. 1693 (2018) 98–108, https://doi.org/10.1016/j.brainres.2018.02.011.

[11] I.R. Mackenzie, R. Rademakers, M. Neumann, TDP-43 and FUS in amyotrophic lateral sclerosis and frontotemporal dementia, Lancet Neurol. 9 (2010) 995–1007, https://doi.org/10.1016/S1474-4422(10)70195-2.

[12] C. Lagier-Tourenne, M. Polymenidou, D.W. Cleveland, TDP-43 and FUS/TLS: emerging roles in RNA processing and neurodegeneration, Hum. Mol. Genet. 19 (2010) R46–R64, https://doi.org/10.1093/hmg/ddq137.

[13] A. Ratti, E. Buratti, Physiological functions and pathobiology of TDP-43 and FUS/TLS proteins, J. Neurochem. 138 (Suppl 1) (2016) 95–111, https://doi.org/10.1111/jnc.13625.

[14] E. Bentmann, C. Haass, D. Dormann, Stress granules in neurodegeneration – lessons learnt from TAR DNA binding protein of 43 kDa and fused in sarcoma, FEBS J. 280 (2013) 4348–4370, https://doi.org/10.1111/febs.12287.

[15] A. Wood, Y. Gurfinkel, N. Polain, W. Lamont, S. Lyn Rea, Molecular mechanisms underlying TDP-43 pathology in cellular and animal models of ALS and FTLD, Int. J. Mol. Sci. 22 (2021) 4705, https://doi.org/10.3390/ijms22094705.

[16] J.C. Mitchell, P. McGoldrick, C. Vance, T. Hortobagyi, J. Sreedharan, B. Rogelj, E.L. Tudor, B.N. Smith, C. Klasen, C.C. Miller, J.D. Cooper, L. Greensmith, C.E. Shaw, Overexpression of human wild-type FUS causes progressive motor neuron degeneration in an age- and dose-dependent fashion, Acta Neuropathol. 125 (2013) 273–288, https://doi.org/10.1007/s00401-012-1043-z.

[17] C. Yang, T. Qiao, J. Yu, H. Wang, Y. Guo, J. Salameh, J. Metterville, S. Parsi, I. Yusuf, R.H. Brown, H. Cai, Z. Xu, Low-level overexpression of wild type TDP-43 causes late-onset, progressive neurodegeneration and paralysis in mice, PLoS One 17 (2022), e0255710, https://doi.org/10.1371/journal.pone.0255710.

[18] T. Philips, J.D. Rothstein, Rodent models of amyotrophic lateral sclerosis, Curr. Protoc. Pharmacol. 69 (2015) 5–67, https://doi.org/10.1002/0471141755.ph0567s69, .1-5.67.21.

[19] P. McGoldrick, P.I. Joyce, E.M. Fisher, L. Greensmith, Rodent models of amyotrophic lateral sclerosis, Biochim. Biophys. Acta 1832 (2013) 1421–1436, https://doi.org/10.1016/j.bbadis.2013.03.012.

[20] M. Sabatelli, A. Moncada, A. Conte, S. Lattante, G. Marangi, M. Luigetti, M. Lucchini, M. Mirabella, A. Romano, A. Del Grande, G. Bisogni, P.N. Doronzio, P.M. Rossini, M. Zollino, Mutations in the 3' untranslated region of FUS causing FUS overexpression are associated with amyotrophic lateral sclerosis, Hum. Mol. Genet. 22 (2013) 4748–4755, https://doi.org/10.1093/hmg/ddt328.

[21] O.D. King, A.D. Gitler, J. Shorter, The tip of the iceberg: RNA-binding proteins with prion-like domains in neurodegenerative disease, Brain Res. 1462 (2012) 61–80, https://doi.org/10.1016/j.brainres.2012.01.016.

[22] B. Portz, B.L. Lee, J. Shorter, FUS and TDP-43 phases in health and disease, Trends Biochem. Sci. 46 (2021) 550–563, https://doi.org/10.1016/j.tibs.2020.12.005.

[23] M. Kato, T.W. Han, S. Xie, K. Shi, X. Du, L.C. Wu, H. Mirzaei, E.J. Goldsmith, J. Longgood, J. Pei, N.V. Grishin, D.E. Frantz, J.W. Schneider, S. Chen, L. Li, M.R. Sawaya, D. Eisenberg, R. Tycko, S.L. McKnight, Cell-free formation of RNA granules: low complexity sequence domains form dynamic fibers within hydrogels, Cell 149 (2012) 753–767, https://doi.org/10.1016/j.cell.2012.04.017.

[24] L. Liu-Yesucevitz, A.Y. Lin, A. Ebata, J.Y. Boon, W. Reid, Y.F. Xu, K. Kobrin, G.J. Murphy, L. Petrucelli, B. Wolozin, ALS-linked mutations enlarge TDP-43-enriched neuronal RNA granules in the dendritic arbor, J. Neurosci. 34 (2014) 4167–4174, https://doi.org/10.1523/JNEUROSCI.2350-13.2014.

[25] S. Loganathan, E.M. Lehmkuhl, R.J. Eck, D.C. Zarnescu, To be or not to be…toxic – is RNA association with TDP-43 complexes deleterious or protective in neurodegeneration? Front. Mol. Biosci. 6 (2020) 154, https://doi.org/10.3389/fmolb.2019.00154, eCollection 2019.

[26] A. Aulas, C. Vande Velde, Alterations in stress granule dynamics driven by TDP-43 and FUS: a link to pathological inclusions in ALS? Front. Cell. Neurosci. 9 (2015) 423, https://doi.org/10.3389/fncel.2015.00423.

[27] M.A. Kiebler, G.J. Bassell, Neuronal RNA granules: movers and makers, Neuron 51 (2006) 685–690, https://doi.org/10.1016/j.neuron.2006.08.021.

[28] R. Fujii, T. Takumi, TLS facilitates transport of mRNA encoding an actin-stabilizing protein to dendritic spines, J. Cell Sci. 118 (2005) 5755–5765, https://doi.org/10.1242/jcs.02692.

[29] H.A. Bowden, D. Dormann, Altered mRNP granule dynamics in FTLD pathogenesis, J. Neurochem. 138 (2016) 112–133, https://doi.org/10.1111/jnc.13601.

[30] V. Rangaraju, S. Tom Dieck, E.M. Schuman, Local translation in neuronal compartments: how local is local? EMBO Rep. 18 (2017) 693–711, https://doi.org/10.15252/embr.201744045.

[31] I.P. Sudhakaran, M. Ramaswami, Long-term memory consolidation: the role of RNA-binding proteins with prion-like domains, RNA Biol. 14 (2017) 568–586, https://doi.org/10.1080/15476286.2016.1244588.

[32] K. Nakayama, R. Ohashi, Y. Shinoda, M. Yamazaki, M. Abe, A. Fujikawa, S. Shigenobu, A. Futatsugi, M. Noda, K. Mikoshiba, T. Furuichi, K. Sakimura, N. Shiina, RNG105/caprin1, an RNA granule protein for dendritic mRNA localization, is essential for long-term memory formation, Elife 6 (2017), e29677, https://doi.org/10.7554/eLife.29677.

[33] N.B. Nedelsky, J.P. Taylor, Pathological phase transitions in ALS-FTD impair dynamic RNA-protein granules, RNA 28 (2022) 97–113, https://doi.org/10.1261/rna.079001.121.

[34] A. Patel, H.O. Lee, L. Jawerth, S. Maharana, M. Jahnel, M.Y. Hein, S. Stoynov, J. Mahamid, S. Saha, T.M. Franzmann, A. Pozniakovski, I. Poser, N. Maghelli, L. A. Royer, M. Weigert, E.W. Myers, S. Grill, D. Drechsel, A.A. Hyman, S. Alberti, A liquid-to-solid phase transition of the ALS protein FUS accelerated by disease mutation, Cell 162 (2015) 1066–1077, https://doi.org/10.1016/j.cell.2015.07.047.

[35] W.M. Babinchak, R. Haider, B.K. Dumm, P. Sarkar, K. Surewicz, J.K. Choi, W.K. Surewicz, The role of liquid-liquid phase separation in aggregation of the TDP-43 low-complexity domain, J. Biol. Chem. 294 (2019) 6306–6317, https://doi.org/10.1074/jbc.RA118.007222.

[36] T. Murakami, S. Qamar, J.Q. Lin, G.S. Schierle, E. Rees, A. Miyashita, A.R. Costa, R.B. Dodd, F.T. Chan, C.H. Michel, D. Kronenberg-Versteeg, Y. Li, S.P. Yang, Y. Wakutani, W. Meadows, R.R. Ferry, L. Dong, G.G. Tartaglia, G. Favrin, W.L. Lin, D.W. Dickson, M. Zhen, D. Ron, G. Schmitt-Ulms, P.E. Fraser, N.A. Shneider, C. Holt, M. Vendruscolo, C.F. Kaminski, P. St George-Hyslop, ALS/FTD mutation-induced phase transition of FUS liquid droplets and reversible hydrogels into irreversible hydrogels impairs RNP granule function, Neuron 88 (2015) 678–690, https://doi.org/10.1016/j.neuron.2015.10.030.

[37] P.P. Gopal, J.J. Nirschl, E. Klinman, E.L. Holzbaur, Amyotrophic lateral sclerosis-linked mutations increase the viscosity of liquid-like TDP-43 RNP granules in neurons, Proc. Natl. Acad. Sci. USA 114 (2017) E2466–E2475, https://doi.org/10.1073/pnas.1614462114.

[38] J.C. Darnell, J.D. Richter, Cytoplasmic RNA-binding proteins and the control of complex brain function, Cold Spring Harbor Perspect. Biol. 4 (2012) a012344, https://doi.org/10.1101/cshperspect.a012344.

[39] R. Roy, N. Shiina, D.O. Wang, More dynamic, more quantitative, unexpectedly intricate: advanced understanding on synaptic RNA localization in learning and memory, Neurobiol. Learn. Mem. 168 (2020), 107149, https://doi.org/10.1016/j.nlm.2019.107149.

[40] C.M. Dewey, B. Cenik, C.F. Sephton, D.R. Dries, P. Mayer 3rd, S.K. Good, B.A. Johnson, J. Herz, G. Yu, TDP-43 is directed to stress granules by sorbitol, a novel physiological osmotic and oxidative stressor, Mol. Cell Biol. 31 (2011) 1098–1108, https://doi.org/10.1128/MCB.01279-10.

[41] E. Kabashi, L. Lin, M.L. Tradewell, P.A. Dion, V. Bercier, P. Bourgouin, D. Rochefort, S. Bel Hadj, H.D. Durham, C. Vande Velde, G.A. Rouleau, P. Drapeau, Gain and loss of function of ALS-related mutations of TARDBP (TDP-43) cause motor deficits *in vivo*, Hum. Mol. Genet. 19 (2010) 671–683, https://doi.org/10.1093/hmg/ddp534.

[42] D. Ito, M. Seki, Y. Tsunoda, H. Uchiyama, N. Suzuki, Nuclear transport impairment of amyotrophic lateral sclerosis-linked mutations in FUS/TLS, Ann. Neurol. 69 (2011) 152–162, https://doi.org/10.1002/ana.22246.

[43] V. Swarup, D. Phaneuf, C. Bareil, J. Robertson, G.A. Rouleau, J. Kriz, J.P. Julien, Pathological hallmarks of amyotrophic lateral sclerosis/frontotemporal lobar degeneration in transgenic mice produced with TDP-43 genomic fragments, Brain 134 (2011) 2610–2626, https://doi.org/10.1093/brain/awr159.

[44] G. Shiihashi, D. Ito, T. Yagi, Y. Nihei, T. Ebine, N. Suzuki, Mislocated FUS is sufficient for gain-of-toxic-function amyotrophic lateral sclerosis phenotypes in mice, Brain 139 (2016) 2380–2394, https://doi.org/10.1093/brain/aww161.

[45] N. Shiina, Liquid- and solid-like RNA granules form through specific scaffold proteins and combine into biphasic granules, J. Biol. Chem. 294 (2019) 3532–3548, https://doi.org/10.1074/jbc.RA118.005423.

[46] R. El Fatimy, S. Tremblay, A.Y. Dury, S. Solomon, P. De Koninck, J.W. Schrader, E.W. Khandjian, Fragile X mental retardation protein interacts with the RNA-binding protein Caprin1 in neuronal RiboNucleoProtein complexes, PLoS One 7 (2012), e39338, https://doi.org/10.1371/journal.pone.0039338.

[47] T.H. Kim, B. Tsang, R.M. Vernon, N. Sonenberg, L.E. Kay, J.D. Forman-Kay, Phospho-dependent phase separation of FMRP and CAPRIN1 recapitulates regulation of translation and deadenylation, Science 365 (2019) 825–829, https://doi.org/10.1126/science.aax4240.

[48] S. Jain, J.R. Wheeler, R.W. Walters, A. Agrawal, A. Barsic, R. Parker, ATPase-modulated stress granules contain a diverse proteome and substructure, Cell 164 (2016) 487–498, https://doi.org/10.1016/j.cell.2015.12.038.

[49] L. Luchelli, M.G. Thomas, G.L. Boccaccio, Synaptic control of mRNA translation by reversible assembly of XRN1 bodies, J. Cell Sci. 128 (2015) 1542–1554, https://doi.org/10.1242/jcs.163295.

[50] N. Shiina, K. Yamaguchi, M. Tokunaga, RNG105 deficiency impairs the dendritic localization of mRNAs for Na^+/K^+ ATPase subunit isoforms and leads to the degeneration of neuronal networks, J. Neurosci. 30 (2010) 12816–12830, https://doi.org/10.1523/JNEUROSCI.6386-09.2010.

[51] C. Wang, B. Han, R. Zhou, X. Zhuang, Real-time imaging of translation on single mRNA transcripts in live cells, Cell 165 (2016) 990–1001, https://doi.org/10.1016/j.cell.2016.04.040.

[52] A.M. Krichevsky, K.S. Kosik, Neuronal RNA granules: a link between RNA localization and stimulation-dependent translation, Neuron 32 (2001) 683–696, https://doi.org/10.1016/s0896-6273(01)00508-6.

[53] P. Majumder, J.F. Chu, B. Chatterjee, K.B. Swamy, C.J. Shen, Co-regulation of mRNA translation by TDP-43 and Fragile X Syndrome protein FMRP, Acta Neuropathol. 132 (2016) 721–738, https://doi.org/10.1007/s00401-016-1603-8.

[54] C. Colombrita, E. Onesto, F. Megiorni, A. Pizzuti, F.E. Baralle, E. Buratti, V. Silani, A. Ratti, TDP-43 and FUS RNA-binding proteins bind distinct sets of cytoplasmic messenger RNAs and differently regulate their post-transcriptional fate in motoneuron-like cells, J. Biol. Chem. 287 (2012) 15635–15647, https://doi.org/10.1074/jbc.M111.333450.

[55] E.M. Tank, C. Figueroa-Romero, L.M. Hinder, K. Bedi, H.C. Archbold, X. Li, K. Weskamp, N. Safren, X. Paez-Colasante, C. Pacut, S. Thumma, M.T. Paulsen, K. Guo, J. Hur, M. Ljungman, E.L. Feldman, S.J. Barmada, Abnormal RNA stability in amyotrophic lateral sclerosis, Nat. Commun. 9 (2018) 2845, https://doi.org/10.1038/s41467-018-05049-z.

[56] N. Shiina, K. Shinkura, M. Tokunaga, A novel RNA-binding protein in neuronal RNA granules: regulatory machinery for local translation, J. Neurosci. 25 (2005) 4420–4434, https://doi.org/10.1523/JNEUROSCI.0382-05.2005.

[57] L. Wickham, T. Duchaîne, M. Luo, I.R. Nabi, L. DesGroseillers, Mammalian staufen is a double-stranded-RNA- and tubulin-binding protein which localizes to the rough endoplasmic reticulum, Mol. Cell Biol. 19 (1999) 2220–2230, https://doi.org/10.1128/MCB.19.3.2220.

[58] T.F. Duchaîne, I. Hemraj, L. Furic, A. Deitinghoff, M.A. Kiebler, L. DesGroseillers, Staufen2 isoforms localize to the somatodendritic domain of neurons and interact with different organelles, J. Cell Sci. 115 (2002) 3285–3295, https://doi.org/10.1242/jcs.115.16.3285.

[59] M. Hallegger, A.M. Chakrabarti, F.C.Y. Lee, B.L. Lee, A.G. Amalietti, H.M. Odeh, K.E. Copley, J.D. Rubien, B. Portz, K. Kuret, I. Huppertz, F. Rau, R. Patani, N. L. Fawzi, J. Shorter, N.M. Luscombe, J. Ule, TDP-43 condensation properties specify its RNA-binding and regulatory repertoire, Cell 184 (2021) 4680–4696, https://doi.org/10.1016/j.cell.2021.07.018, e22.

[60] A. Khong, T. Matheny, S. Jain, S.F. Mitchell, J.R. Wheeler, R. Parker, The stress granule transcriptome reveals principles of mRNA accumulation in stress granules, Mol. Cell. 68 (2017) 808–820, https://doi.org/10.1016/j.molcel.2017.10.015, e5.

[61] C. Vance, E.L. Scotter, A.L. Nishimura, C. Troakes, J.C. Mitchell, C. Kathe, H. Urwin, C. Manser, C.C. Miller, T. Hortobágyi, M. Dragunow, B. Rogelj, C.E. Shaw, ALS mutant FUS disrupts nuclear localization and sequesters wild-type FUS within cytoplasmic stress granules, Hum. Mol. Genet. 22 (2013) 2676–2688, https://doi.org/10.1093/hmg/ddt117.

[62] T. Nomura, S. Watanabe, K. Kaneko, K. Yamanaka, N. Nukina, Y. Furukawa, Intranuclear aggregation of mutant FUS/TLS as a molecular pathomechanism of amyotrophic lateral sclerosis, J. Biol. Chem. 289 (2014) 1192–1202, https://doi.org/10.1074/jbc.M113.516492.

[63] D. Dormann, R. Rodde, D. Edbauer, E. Bentmann, I. Fischer, A. Hruscha, M.E. Than, I.R. Mackenzie, A. Capell, B. Schmid, M. Neumann, C. Haass, ALS-associated fused in sarcoma (FUS) mutations disrupt Transportin-mediated nuclear import, EMBO J. 29 (2010) 2841–2857, https://doi.org/10.1038/emboj.2010.143.

[64] Q. Ding, J. Chaplin, M.J. Morris, M.A. Hilliard, E. Wolvetang, D.C.H. Ng, P.G. Noakes, TDP-43 mutation affects stress granule dynamics in differentiated NSC-34 motoneuron-like cells, Front. Cell Dev. Biol. 9 (2021), 611601, https://doi.org/10.3389/fcell.2021.611601.

[65] S. Watanabe, K. Oiwa, Y. Murata, O. Komine, A. Sobue, F. Endo, E. Takahashi, K. Yamanaka, ALS-linked TDP-43^{M337V} knock-in mice exhibit splicing deregulation without neurodegeneration, Mol. Brain 13 (2020) 8, https://doi.org/10.1186/s13041-020-0550-4.

[66] A. Sharma, A.K. Lyashchenko, L. Lu, S.E. Nasrabady, M. Elmaleh, M. Mendelsohn, A. Nemes, J.C. Tapia, G.Z. Mentis, N.A. Shneider, ALS-associated mutant FUS induces selective motor neuron degeneration through toxic gain of function, Nat. Commun. 7 (2016), 10465, https://doi.org/10.1038/ncomms10465.

[67] A. Wang, A.E. Conicella, H.B. Schmidt, E.W. Martin, S.N. Rhoads, A.N. Reeb, A. Nourse, D. Ramirez Montero, V.H. Ryan, R. Rohatgi, F. Shewmaker, M.T. Naik, T. Mittag, Y.M. Ayala, N.L. Fawzi, A single N-terminal phosphomimic disrupts TDP-43 polymerization, phase separation, and RNA splicing, EMBO J. 37 (2018), e97452, https://doi.org/10.15252/embj.201797452.

[68] Y. Shin, J. Berry, N. Pannucci, M.P. Haataja, J.E. Toettcher, C.P. Brangwynne, Spatiotemporal control of intracellular phase transitions using light-activated optoDroplets, Cell 168 (2017) 159–171.e14, https://doi.org/10.1016/j.cell.2016.11.054.

[69] S. Alberti, A. Gladfelter, T. Mittag, Considerations and challenges in studying liquid-liquid phase separation and biomolecular condensates, Cell 176 (2019) 419–434, https://doi.org/10.1016/j.cell.2018.12.035.

[70] S.F. Banani, H.O. Lee, A.A. Hyman, M.K. Rosen, Biomolecular condensates: organizers of cellular biochemistry, Nat. Rev. Mol. Cell Biol. 18 (2017) 285–298, https://doi.org/10.1038/nrm.2017.7.

[71] A. Padrón, N. Ingolia, Analyzing the composition and organization of ribonucleoprotein complexes by APEX-Seq, Methods Mol. Biol. 2428 (2022) 277–289, https://doi.org/10.1007/978-1-0716-1975-9_17.

[72] M. Honda, S. Oki, R. Kimura, A. Harada, K. Maehara, K. Tanaka, C. Meno, Y. Ohkawa, High-depth spatial transcriptome analysis by photo-isolation chemistry, Nat. Commun. 12 (2021) 4416, https://doi.org/10.1038/s41467-021-24691-8.

[73] C. Huang, H. Zhou, J. Tong, H. Chen, Y.J. Liu, D. Wang, X. Wei, X.G. Xia, FUS transgenic rats develop the phenotypes of amyotrophic lateral sclerosis and frontotemporal lobar degeneration, PLoS Genet. 7 (2011), e1002011, https://doi.org/10.1371/journal.pgen.1002011.

[74] K.J. Tsai, C.H. Yang, Y.H. Fang, K.H. Cho, W.L. Chien, W.T. Wang, T.W. Wu, C.P. Lin, W.M. Fu, C.K. Shen, Elevated expression of TDP-43 in the forebrain of mice is sufficient to cause neurological and pathological phenotypes mimicking FTLD-U, J. Exp. Med. 207 (2010) 1661–1673, https://doi.org/10.1084/jem.20092164.

[75] P.R. Silva, G.V. Nieva, L.M. Igaz, Suppression of conditional TDP-43 transgene expression differentially affects early cognitive and social phenotypes in TDP-43 mice, Front. Genet. 10 (2019) 369, https://doi.org/10.3389/fgene.2019.00369.

[76] K. Takahashi, N. Yoshida, N. Murakami, K. Kawata, H. Ishizaki, M. Tanaka-Okamoto, J. Miyoshi, A.R. Zinn, H. Shime, N. Inoue, Dynamic regulation of p53 subnuclear localization and senescence by MORC3, Mol. Biol. Cell 18 (2007) 1701–1709, https://doi.org/10.1091/mbc.e06-08-0747.

[77] R.M. Marión, P. Fortes, A. Beloso, C. Dotti, J. Ortín, A human sequence homologue of Staufen is an RNA-binding protein that is associated with polysomes and localizes to the rough endoplasmic reticulum, Mol. Cell Biol. 19 (1999) 2212–2219, https://doi.org/10.1128/MCB.19.3.2212.

[78] Z. Wang, X. Jiao, A. Carr-Schmid, M. Kiledjian, The hDcp2 protein is a mammalian mRNA decapping enzyme, Proc. Natl. Acad. Sci. USA 99 (2002) 12663–12668, https://doi.org/10.1073/pnas.192445599.

[79] V.I. Bashkirov, H. Scherthan, J.A. Solinger, J.M. Buerstedde, W.D. Heyer, A mouse cytoplasmic exoribonuclease (mXRN1p) with preference for G4 tetraplex substrates, J. Cell Biol. 136 (1997) 761–773, https://doi.org/10.1083/jcb.136.4.761.

[80] L.H. Lo, R. Dong, Q. Lyu, K.O. Lai, The protein arginine methyltransferase PRMT8 and substrate G3BP1 control Rac1-PAK1 signaling and actin cytoskeleton for dendritic spine maturation, Cell Rep. 31 (2020), 107744, https://doi.org/10.1016/j.celrep.2020.107744.

[81] Z. Liang, Y. Zhan, Y. Shen, C.C. Wong, J.R. Yates 3rd, F. Plattner, K.O. Lai, N.Y. Ip, The pseudokinase CaMKv is required for the activity-dependent maintenance of dendritic spines, Nat. Commun. 7 (2016) 13282, https://doi.org/10.1038/ncomms13282.